Mn-Modified Polypyrrole Thin Films for Supercapacitor Electrodes

by

Purnama Ningsih, Clovia Z. Holdsworth, Scott W. Donne*

Discipline of Chemistry, University of Newcastle, Callaghan NSW 2308, Australia

Abstract

Thin film Mn-modified polypyrrole (PPy) composite electrodes have been prepared by chronoamperometric electrodeposition and characterized in terms of their physico-chemical and electrochemical properties and performance. Analysis of the chronoamperometric data shows that electrodeposition of the thin film results in a relative increase in electrochemically active surface area of up to 30 times. This finding was supported by transmission electron microscopy (TEM), atomic force microscopy (AFM) and profilometry analysis of the films. Electrochemical quartz crystal microbalance (EQCM) studies have allowed for the direct determination of electrode mass, both during deposition and electrochemical performance evaluation, which has enabled analysis of electrode properties, including film growth (up to 26 μg/cm^2), density (~2 g/cm^3), and the charge storage during electrochemical cycling, including the rates of mass uptake/removal with charge. The characteristics of the composite electrodes were compared with PPy-only electrodes throughout.

Keywords: polypyrrole; manganese oxides; supercapacitor electrode materials; electrochemical quartz crystal microbalance; atomic force microscopy

* Communicating author

Ph: +61 2 4921 5477; Fax: +61 2 4921 5472; Email: scott.donne@newcastle.edu.au

1. INTRODUCTION

1.1. Energy Storage in Supercapacitor Systems

Nowadays energy has emerged as a fundamental focus for major world economic powers and a great challenge for the scientific community [1]. Energy storage systems have in the past, and will continue to do so into the future, play a significant role in consumer electronics. They also have an emerging role in transportation, where the introduction of electric and hybrid electric vehicles is growing in popularity, and in grid energy storage, where they are an important complement to renewable energy production systems.

In this work our focus is on the use of supercapacitors for energy storage. The relative performance of supercapacitors compared to batteries and fuel cells can be summarized by a typical Ragone diagram [2]. Supercapacitors are typified by a high specific power output but a low specific energy density, which has unfortunately inhibited their widespread commercialization. Another distinct advantage that supercapacitors possess compared to the other types of energy storage devices is their cyclability, which is typically of the order of $>10^5$ cycles, compared to $\sim10^3$ for batteries. Considerable research in recent times has gone into improving the specific energy of supercapacitor electrode materials and devices, with the intent of also retaining their high specific power and excellent cyclability (for example [3-5]). Such developments will provide greater energy storage options for consumers.

1.2. Supercapacitor Charge Storage Mechanisms and Materials

Present day commercial supercapacitors typically employ a symmetrical geometry, in which both electrodes are based on high surface area carbons such as activated carbon, carbon fibres, aerogels, xerogels, fullerenes, and other various nanostructures [6, 7]. The electrolyte in such systems is either a non-aqueous or aqueous electrolyte; e.g., 1 M tetraethylammonium tetrafluoroborate in acetonitrile or aqueous 1 M H_2SO_4, respectively. Energy storage in such devices occurs by charge separation at the solid-electrolyte interface within the porous electrode structure

[8]. As a result of the use of a high surface area carbon materials, considerable charge can be stored; i.e., up to 300 F/g [8-10]. Furthermore, since no physical or chemical changes are occurring in the electrode with such a process, such systems exhibit excellent cyclability.

An alternative approach to charge storage in supercapacitor systems is to employ pseudo-capacitance, which is essentially the use of fast and reversible surface or near surface redox reactions [11]. Such an approach is a common strategy for improving specific capacitance due to the fact that more than just the surface of the material is being utilized for charge storage. Classes of materials that exhibit pseudo-capacitance include conductive polymers and metal oxides, with this latter class of materials crossing the boundary between battery and supercapacitor domains [12, 13]. An excellent recent review of materials for supercapacitors by Naoi and Simon can be found in reference [13].

Conducting polymers that have been examined as supercapacitor electrode materials include polyaniline, polypyrrole and polythiophene, together with their many derivatives [14]. The specific capacitance of such materials has been reported to range up to ~300 F/g, with energy storage again occurring via charge separation at the conductive polymer-electrolyte interface [15]. One of the main drawbacks of these systems, however, is their poor mechanical stability after repeated cycling [16].

The prototypical metal oxide that has been examined as a supercapacitor electrode is hydrated amorphous ruthenium dioxide, which has been reported to have a specific capacitance of up to 1200 F/g [17, 18]. While an excellent performing material, its high cost and toxicity has limited its widespread commercial uptake. As reported by Naoi and Simon, other metal oxides that have been examined include manganese, nickel, tin, and iron oxides [13]. Of these, it is apparent that manganese oxides have considerable potential as supercapacitor electrode materials, exhibiting good electrochemical performance (up to 800 F/g [13]), as well as being of low cost and toxicity. Recent reports from our own laboratory have shown that electrodeposited thin films of manganese dioxide exhibit excellent specific capacitances of over 2000 F/g in an aqueous 0.5 M Na_2SO_4

electrolyte [19]. This level of performance has been ascribed to the use of a high surface area active material exhibiting both pseudo-capacitance and charge separation at the solid-electrolyte interface.

1.3. This Work

In the vast majority of work reported previously in the literature, the materials being examined have been prepared as free flowing powders, which were then cast into electrodes on a suitable conducting substrate. It is relatively rare that thin films of manganese dioxide, or any electro-active material for that matter, are deposited onto a substrate which was then used immediately as the supercapacitor electrode. This approach has considerable advantages, not only in terms of performance, but also in terms of ease of processing. A number of researchers have used electrodeposition to produce polypyrrole, manganese dioxide, and composites thereof (e.g., references [20-25]); however, relatively thick deposits were studied in these reports which has ultimately influenced the performance results, making the electrodeposited films comparable in performance to powdered materials.

Conducting polymers such as polypyrrole can also be prepared via electrodeposition (e.g., [26]); however, similar to the electrodes prepared from powdered materials, their mechanical instability causes a breakdown in electrode performance [27]. In this work we will examine the electrochemical deposition of polypyrrole that has been modified by the presence of Mn^{2+}, with the intent of stabilizing the polypyrrole during cycling. Additionally, we will also demonstrate that enhanced electrode performance from these composites can be achieved through the use of thin film electrodeposition.

2. EXPERIMENTAL

2.1. Materials

The materials used in this study for the synthesis of the electrode composites were the pyrrole

monomer (Py; Merck; 99%), $MnSO_4.H_2O$ (Sigma-Aldrich; >99%) and H_2SO_4 (Sigma-Aldich; 98%). Experiments to evaluate the electrochemical performance of our electrodes employed an aqueous solution of K_2SO_4 (Sigma-Aldrich; >99%). All aqueous solutions prepared in this study made use of Milli-Q ultra pure water (resistivity >18.2 MΩ.cm).

2.2. Electrochemical Protocols

All electrochemical experiments were conducted using a Stanford Research Systems QCM200 as an electrochemical quartz crystal microbalance (EQCM). In this case the working electrode was a 1.325 cm^2 platinum disk sputter coated on a 5 MHz resonant frequency quartz crystal. Prior to use, this platinum electrode was cleaned by immersion in a 0.1 M H_2SO_4 + 5% H_2O_2 solution. This was used in conjunction with a saturated calomel reference electrode (SCE), against which all potentials were measured and reported, and a graphite rod counter electrode (6.3 cm^2). All electrochemical experiments were controlled using a Perkin Elmer VMP multi-channel potentiostat/galvanostat with ECLab software.

Electrodeposition experiments were carried out using aqueous solutions containing combinations of Py (0, 0.001, 0.01 or 0.1 M), $MnSO_4.H_2O$ (0, 0.001, 0.01 or 0.1 M) and 0.1 M H_2SO_4. All electrodeposition experiments were carried out using chronoamperometry, although prior to this a linear sweep voltammetry experiment was conducted on each solution being studied so as to identify an appropriate step potential. Once this potential had been identified, and after the platinum substrate had been cleaned again in 0.1 M H_2SO_4 + 5% H_2O_2, each chronoamperometry experiment was carried out for 30 s.

After each chronoamperometric deposition, the coated quartz EQCM electrode was rinsed thoroughly with Milli-Q water to remove any associated plating electrolyte. Without being dried the electrode was then immersed into a 0.1 M K_2SO_4 solution, together with the same SCE reference and graphite counter electrodes as used previously. This electrode was then cycled for at least 50 cycles between 0.0-1.0 V versus SCE at a rate of 5 mV/s.

The Pt working electrode was used for electrochemical impedance spectroscopy work (EIS) work. After each electrodeposition, the Pt working electrode was rinsed H_2O and without being dried the electrode was then immersed into a 0.1 M K_2SO_4 solution, together with the same SCE reference and graphite counter electrodes in an EIS system by using the combination of a Solartron 1254 Frequency Response Analyzer and a Solartron 1287 Electrochemical Interface controlled by ZPlot software. From the open circuit voltage of the thin films electrode (0.300 V) the voltage was stepped in the anodic direction 25 mV, after which it was allowed to equilibrate for a period of 10 min. After this, an impedance spectrum on the thin films electrode was measured using the frequency range 20 kHz to 0.1 Hz and a 10 mV excitation signal. This sequence was repeated to the upper voltage limit (1.0 V versus SCE), down to the lower voltage limit (0.0 V versus SCE), and then once more back up to the upper voltage limit. The resultant impedance spectra were then interpreted using an appropriate equivalent circuit.

2.3. Morphological Characterization

Owing to the nature of the very thin films of electrodeposited material, morphological characterization is quite challenging. Traditional methods of analysis such as X-ray diffraction and scanning electron microscopy (SEM) are not possible due to the limited amount of material present. Despite this, lengthening the deposition time to make a thicker deposit has shown that the material is still amorphous to X-ray diffraction [19]. There are however, concerns about this approach because of changes in the nature of the deposit using the chronoamperometric method. Nevertheless, for morphological characterization in this study the samples were examined by atomic force microscopy (AFM; Asylum Research Cypher Scanning Probe Microscope) in AC mode with a 2.44 Hz scan rate, transmission electron microscopy (TEM; JEOL JEM-1200EXII) on samples scraped off the platinum substrate, and surface profilimetry (KLA Tencor Alfa Step-500) after scratching the film in a small area to expose the platinum substrate.

2.4. Chemical Composition

Separate films were also prepared for compositional analysis to determine the relative amounts of polypyrrole (PPy) and manganese in each film. To achieve this, each film was first thoroughly washed with Milli-Q ultra-pure water to remove any residual electrolyte and then digested in 30 mL of 0.1 M H_2SO_4 + 5% H_2O_2 to essentially extract the manganese from the film. Each extract solution was then transferred to its own 100 mL volumetric flask, which was made up to volume using Milli-Q water. These solutions were then aspirated into a Varian Liberty Series II ICP-OES instrument to determine the manganese concentration. Matrix matched standard solutions were prepared from $MnSO_4.H_2O$ and H_2SO_4.

3. RESULTS AND DISCUSSION

3.1. Linear Sweep Voltammetry

Figure 1 compares the anodic voltametric behaviour of solutions containing 0.1 M Py + 0.1 M H_2SO_4, 0.1 M Mn^{2+} + 0.1 M H_2SO_4 and 0.1 M Py + 0.1 M Mn^{2+} + 0.1 M H_2SO_4 scanned at 5 mV/s. The behaviour of the 0.1 M Mn^{2+} + 0.1 M H_2SO_4 solution consists of a voltametric wave starting at ~1.08 V, which is followed by oxygen evolution at higher potentials. This behaviour is typical of that expected for such an electrolyte [19]. Oxidation of Mn^{2+} in this case occurs via the reaction

$$Mn^{2+} + 2H_2O \rightarrow MnO_2 + 4H^+ + 2e^- \quad ...(1)$$

However, the mechanism of oxidation is not so straightforward.

Figure 2 summarizes the possible Mn^{2+} oxidation pathways to form MnO_2 that have been reported in the literature [19]. The first step in the process is the single electron oxidation of Mn^{2+} to form a soluble Mn^{3+} intermediate. The acidity of the electrolyte then determines which pathway predominates. In more concentrated acidic electrolytes (Path C) the Mn^{3+} intermediate has a reasonable stability, meaning that it can disproportionate with another Mn^{3+} species to form soluble Mn^{2+} and Mn^{4+}, the latter of which hydrolyzes immediately to precipitate MnO_2 on the electrode

substrate. However, if the electrolyte is not so concentrated in acid (Path A), then the Mn^{3+} intermediate is not so stable, hydrolyzing to precipitate a solid Mn(III) species (such as MnOOH) on the electrode surface, which can be subsequently oxidized in the solid state to form MnO_2. There is the possibility of a direct two-electron oxidation of Mn^{2+} to MnO_2 (Path B); however, there is no evidence in the literature to support the occurrence of this process. Certainly no one process occurs individually, but rather the combination of processes is shifted one way or the other depending on the exact electrolyte conditions.

The anodic polymerization of Py in Figure 1 began at a potential of ~0.54 V, and exhibited a sharp increase in current, so much so that diffusion limited conditions were not encountered before a current maximum was reached with the potentiostat. It was also noted that increasing the concentration of Py in the electrolyte cause a cathodic shift in the onset potential for PPy formation. This was to be expected based on Nernst equation considerations. In this case, oxidation of Py occurs via the process

$$Py \rightarrow Py^{+\bullet} + e^{-} \qquad ...(2)$$

with the cationic radical acting as the initiator for the polymerization process; i.e.,

$$n(Py^{+\bullet}) \rightarrow (Py)_n + nH^{+} \qquad ...(3)$$

where the resultant polymer (polypyrrole; PPy) is deposited onto the anodic substrate.

For the mixed electrolyte containing both Py and Mn^{2+} the voltametric behaviour appears essentially as a combination of the individual Py and Mn^{2+} i-V profiles, particularly in terms of the main onset potentials for oxidation. For this electrolyte there is also significant current flowing at potentials more cathodic compared to the main onset peak for Py oxidation; i.e., <0.54 V. The current flowing in this region is much higher than either of the other electrolytes, which may indicate some favourable interactions between the Py monomer and the Mn^{2+} ions leading to effectively under-potential deposition of the composite electrode material. As an additional point, from the lower current response in the combined electrolyte, it would seem as though the presence of Mn^{2+} has had an effect on the oxidation of Py, possibly through surface adsorption, that has

inhibited the continued oxidation of the Py. From the data in Figure 1, a potential of 0.75 V versus SCE was chosen as an appropriate potential to carry out chronamperometry experiments to deposit thin films of PPy with and without the presence of Mn^{2+}. This potential was chosen based on previous work from our laboratory [19] which has demonstrated that relatively low potentials, corresponding to non-diffusion limited conditions, gives rise to superior performing electrodes. Furthermore, this potential is also not too high such that the irreversible over-oxidation of PPy occurs [27].

3.2. Chronoamperometric Deposition and Mass Analysis

Figure 3 compares the chronoamperometric responses obtained from the 0.001 Py + 0.001 M Mn^{2+}, 0.01 M Py + 0.01 M Mn^{2+} and 0.1 M Py + 0.1 M Mn^{2+} electrolytes in 0.1 M H_2SO_4. The data shows quite interesting behaviour, very different from what is expected from a typical chronoamperometric deposition; i.e., Cottrell equation behaviour, $i \propto t^{-½}$ [28]. Deposition from solutions containing low concentrations of Py and Mn^{2+} exhibited behaviour that could be regarded as being the closest to expected; however, even in these circumstances an increase in current towards the latter stages of deposition was observed. As the solution concentration of electroactive species increased, this non-Cottrell behaviour was also enhanced. The origin of this behaviour is due to an increasing electrode area as a result of ongoing electrodeposition, through nucleation and growth phenomena, as has been described in earlier literature (e.g., [29]). In this earlier literature the focus has been on extracting rate constants for both crystal nucleation and growth for metals, salts and polymers, albeit in the absence of mass transport considerations, which is of considerable importance here. The focus of the work presented here is on the increase in electrode area as a result of the electrodeposition of PPy.

To examine this further, let us first consider the mechanism of electrodeposition ongoing in this situation. In the time frame immediately after application of the potential step the Py monomer is oxidized to produce a soluble reaction intermediate, as described previously. In this case we

would expect conventional Cottrell i-t behaviour; i.e.,

$$i = \frac{nFACD^{1/2}}{(\pi t)^{1/2}} \qquad ...(4)$$

where i is the current (A), n is the stoichiometric number of electrons flowing in the redox reaction, F is Faraday's constant (96486.7 C/mol), A is the electrochemically active electrode area (m^2), C is the electroactive species concentration (mol/m^3), D is the diffusion coefficient of electroactive species in the electrolyte (m^2/s), and t is the time since onset of the potential step. Figure 4 demonstrates the fitting of the Cottrell equation to the early stages of the chronoamperometric deposition.

The concentration of Py in the initial solution determines the concentration of the intermediate $Py^{+\bullet}$ in the immediate vicinity of the electrode surface (note at this step potential Mn^{2+} is not electroactive), which with time and continued oxidation, increases to a critical saturation level, at which point deposition of the solid products begins; i.e., the $Py^{+\bullet}$ radical initiates polymerization to form polypyrrole (PPy). The mechanism of this polymerization is as follows:

$Py \rightarrow Py^{+\bullet} + e^-$ Initiation ...(5)

$Py^{+\bullet} + Py^{+\bullet} \rightarrow Py^+—Py^+ \rightarrow Py—Py + 2H^+$ …(6)

$Py—Py \rightarrow Py—Py^{+\bullet} + e^-$ Initiation …(7)

$Py—Py^{+\bullet} + Py—Py^{+\bullet} \rightarrow Py—Py—Py—Py + 2H^+$ …(8)

$n(Py) \rightarrow (Py)_n + nH^+ + ne^-$ Overall …(9)

The presence of Mn^{2+}, as indicated in the linear sweep voltammetry data, serves to modify PPy deposition probably through adsorption. The electrode area begins to increase, thus giving rise to an increased current even though mass transport to the electrode surface is constant (diffusion limited current). By comparing the actual current measured (i_{exp}) in the experiment to that predicted from the Cottrell equation (i_{pred}), an estimate of the increase in electrode area can be made; i.e., i_{exp}/i_{pred}, as shown in Figure 5. This comparison is valid because all other parameters in the

Cottrell equation remain constant, except the area.

From Figure 5 it is quite obvious that a dramatic increase in electrode area has occurred above and beyond the initial platinum electrode area (determined by linear sweep voltammetry [28] on the well-behaved and reversible $[Fe(CN)_6]^{3-/4-}$ redox couple in KNO_3 electrolytes). Furthermore, as expected, this area increases with an increasing concentration of electroactive species; e.g., for the most concentrated electrolyte studied, the electrode area was found to increase by up to 30 times over the course of the 30 s deposition. The origin of this increased electrochemically active area is a combination of the high number of nucleation sites for the composite, as well as porosity in the electrodeposited film. Irrespective of the origin of the increased electrode area, this is a promising sign in terms of the electrochemical activity of the composite electrodes because of the inherent increase in specific capacity with electrochemically active area.

Since all the electrodeposition experiments were conducted using the EQCM, the mass of material deposited onto the platinum substrate is immediately available. Figure 6(a) shows a sample massogram, as compared to its chronoamperometric data, in this case for 0.01 M Py + 0.01 M Mn^{2+} + 0.1 M H_2SO_4. The massogram in this figure shows a continual increase in mass, with little induction time evident, indicating that polymerization and deposition were essentially instantaneous after the onset of the step potential. Table 1 lists the final electrode mass after a 30 s deposition as a function of the electrodeposition conditions. As expected from the chronoamperometric data, higher electrode masses were observed when the electrolyte was more concentrated in electroactive species (as indicated by the total charge passed during the chronoamperometric deposition). Table 1 also contains the corresponding data for electrodeposition experiments carried out with just Py as the electroactive species (no Mn^{2+} present). Across all experiments the electrode mass was less when Mn^{2+} was included in the electrolyte. The implication of this is that the presence of Mn^{2+} affects the electrodeposition process, as was noted previously in the linear sweep voltammetry data. An explanation for this is that the relative area of the PPy only electrodes is greater than those prepared in the presence of Mn^{2+}, with the greater area facilitating the deposition of more active material.

Table 1 also contains the predicted area increase for all these electrodes, and apart from the lowest concentration electrolyte, the relative increase in area was similar irrespective of whether Mn^{2+} was present or not. This infers that the Mn^{2+} influences the deposition mechanism of PPy directly, rather than through morphological changes.

Figure 6(b) combines the massogram data with the charge calculated by integration of the chronoamperometric i-t data. As can be seen, this comparison is essentially linear for each of the different electrolytes considered. This data also allows determination of the rate of mass (m; μg) accumulation as a function of charge (Q; C) passed (i.e., dm/dQ), which can provide insight into the nature of the deposited material. Table 1 lists the values for dm/dQ for the various deposits considered here. In all except one instance, the value of dm/dQ was consistent at ~320 μg/C, with a slight trend towards a higher value for the more dilute electrolytes. The exception was the case for 0.001 M Py + 0.001 M Mn^{2+}, in which case dm/dQ was 943 μg/C, almost triple that obtained from the other electrodes. This result, while surprising, was consistent, with three similar experiments repeated to give the same result. Unfortunately, the origin of this much higher value is unknown at this time.

The magnitude of the dm/dQ data can also be used to examine the nature of the deposited product. For instance, electrodeposition of PPy via Eqns (2) and (3) is expected to produce a dm/dQ value of 674 μg/C, which is much larger than that obtained for the majority of experiments. For the electrodeposition of manganese dioxide we expect dm/dQ to be 451 μg/C, which could contribute to lowering the overall value; however, as we have already indicated, manganese dioxide is not be electrodeposited here because the potential we have used is too low, and as such any manganese inclusion is by adsorption, which should have the effect of increasing the value of dm/dQ because the mass should increase without any passage of current. In fact, the only possible reason how the measured value of dm/dQ is less than the expected value is if a fraction of the electrochemically generated species is lost to the electrolyte, and does not contribute to mass build up on the electrode. This could occur as a result of the electro-generated intermediate species $Py^{+\bullet}$ diffusing

away from the electrode surface into the bulk electrolyte, or perhaps more likely, the $Py^{+\bullet}$ species undergoing a decomposition reaction with the solvent water to reform Py. Assuming this last scenario to be the case, the implication is that only ~33% of the charge passed leads to polymerization.

3.3. Chemical and Morphological Characterization

3.3.1. Chemical Composition

As a composite electrodeposited material it is important to know the amount of manganese within the film. To extract this information each composite film was first washed to remove any residual electrolyte and then extracted with acidified H_2O_2 to dissolve and extract any manganese associated with the film. The manganese liberated into solution (as Mn^{2+}) was then analysed by ICP-OES, with the result then expressed as total manganese in the electrode film ($\mu g/cm^2$; Table 1). Overall, the incorporation of manganese into the PPy films closely matched the Mn^{2+} concentration in the starting electrolyte, with a 10-fold increase in Mn^{2+} leading to an approximate 10-fold increase in manganese inclusion in the film. The only exception is the most concentrated electrolyte, in which case a slightly lower level of manganese inclusion was noted, possibly due to saturation of the PPy surface.

3.3.2. Transmission Electron Microscopy (TEM)

Conventional scanning electron microscope (SEM) analysis is not possible for the electrodes prepared in this study due to their very thin nature. Even a TEM analysis is not straightforward due to the fact that the active material is strongly adherent to the platinum substrate. Nevertheless, our approach to the TEM analysis of these electrode films was to deposit an electrode from the 0.1 M Py + 0.1 M Mn^{2+} + 0.1 M H_2SO_4 electrolyte for a longer time (2 min), after which the resultant film could be prised off the substrate surface (carefully) using a scalpel. This material was then dried in air at ambient temperature before being mounted into the TEM for analysis. Figure 7 shows a

typical image of the thin film. It is clear that most of the particle under examination is semi-transparent to the electron beam indicating that the bulk of the deposit is PPy. However, there are some much smaller (<50 nm) darker regions dispersed randomly throughout the film that are not transparent, which are crystals of a manganese oxide. The nature of the manganese oxide present is unknown, but is likely to be a higher valent manganese oxide such as Mn_3O_4 or MnO_2, as a result of partial oxidation of the Mn^{2+} present by the oxygen in air. The appearance of this deposit implies that the crystals of manganese oxide are much denser than that of the PPy.

3.3.3. Atomic Force Microscopy (AFM) and Profilometry

As mentioned above, direct SEM analysis of the electrodeposited thin films was not possible due to their thin nature, and hence the difficulty in differentiating their morphology from that of the platinum substrate. Therefore, AFM was used to characterize the morphology of the thin electrode films prepared in this study. Figure 8 shows typical AFM images (in semi-profile and plan views) obtained from each of the composite films. Note the vertical scale shown in each of the images. It shows quite clearly that as the concentration of electroactive species in the electrolyte increased, so too did the roughness and thickness of the film. The morphology of each of the films appears to consist of small crystallites extending from the substrate, with the occasional larger crystallite protruding further from the surface. What is also apparent, particularly for the most concentrated electrolyte, is that the size of the crystallites has increased. The implication here being that under the most concentrated electrolyte conditions used, crystallite nucleation has been superceded slightly by crystallite growth during deposition. The relative surface area data in Table 1 somewhat reflects this through the diminishing increase in surface area as the electrolyte concentration is increased, as shown in Figure 9. The inset in this figure shows that the relative electrode area increases approximately logarithmically with electrolyte concentration.

Further digital analysis of the AFM images allows for the determination of surface roughness. Table 2 compares the root mean square (RMS) roughness of the composite electrode films

prepared. Essentially this is a measure of the fluctuation in the surface of the deposit. The data in Table 2, in support of the AFM images in Figure 8, shows that there is greater roughness in the deposits produced from the more concentrated electrolytes.

The thickness of the films prepared in this study was examined by profilometry, with the resultant data also shown in Table 2. Note that the thinnest film was unable to be examined using this method. As expected, the thickest deposit was produced from the most concentrated electrolyte. Using the thickness data from profilometry, and the mass data from Table 1, the film density can be calculated, as also shown in Table 2. The literature suggests the density of PPy is 1.48 g/cm^3 [30], which implies that the presence of manganese in the films has increased the overall electrode density, likely via the fact that manganese oxides are inherently denser than PPy [31]. This conclusion is supported by the TEM image shown in Figure 7, where the much denser manganese oxide crystallites are apparent, as is the absence of any appreciable porosity in the PPy film.

3.4. Electrode Performance

3.4.1. Voltammetry

The ultimate test of any energy storage material is its ability to store charge under typical cell conditions. As such, each of the electrode materials prepared in this study were cycled between the potential limits of 0.0-1.0 V versus SCE in an electrolyte of 0.1 M K_2SO_4 at a rate of 5 mV/s for at least 50 cycles. Voltametric data obtained from the Mn-modified PPy electrodes and the PPy-only electrodes are shown in Figure 10, in this case for the 50th cycle. What is apparent firstly is that there is a large cathodic peak present in the potential range 0.13-0.08 V, with the peak shifting to lower potentials with an increasing deposition electrolyte concentration of Py and Mn^{2+}. The likely origin of this cathodic peak is reduction of the PPy film, with the injected charge being recovered during the anodic potential sweep; i.e.,

$$PPy + ne^- \leftrightarrow PPy^{n-} \quad ...(10)$$

For the electrode prepared from the 0.1 M Py + 0.1 M Mn^{2+} electrolyte, there is also a small

cathodic peak at ~0.59 V. This peak is typical of manganese dioxide electrochemical behaviour [19], with the difference between this and the corresponding PPy only electrode confirming this. Aside from these cathodic peaks, there are no other significant processes occurring, except at high potentials where the anodic current begins to tail upwards. Otherwise, in the intermediate potential range, the electrode exhibits behaviour typical of a capacitor; i.e., a relatively constant current over the potential range scanned due to ionic adsorption and desorption phenomena occurring on the PPy film surface.

3.4.2. Cycle Stability and Performance

The specific capacitance of the Mn-modified PPy electrodes over the course of 50 cycles is shown in Figure 11. The focus of this part of the study is to more understand the intrinsic properties of the deposits, and as such that is why we have used a relatively slow scan rate. Higher scan rates tend to focus more on the electrode construction itself, which is not the intent of this work. Furthermore, we have also demonstrated previously for a powdered manganese dioxide electrode, that a slow scan rate also exacerbates any failure mechanisms within the electrode [32], and so enables a much earlier indication as to whether the electrode will be stable over extended cycling. From the data in Figure 11 it is clear that electrodes produced from the most dilute 0.001 M Py + 0.001 M Mn^{2+} electrolyte exhibited an excellent performance of over 2000 F/g during the course of electrode cycling. The specific capacitance was much lower when the electrodes were made from more concentrated electrolytes, most likely due to the preparation of a film with relatively less of the active material exposed to the electrolyte, and hence less of it available for use as an electrochemically active material. Additionally, the specific capacitance from the electrodes remained essentially constant after a small initial decrease. As seen in the inset in Figure 11, the stability of both the Mn-modified PPy and PPy-only electrodes is similar, although the presence of Mn^{2+} during electrodeposition dramatically increases the specific capacitance of the resultant electrode material. Table 1 also contains the average specific capacitance over the last 30 cycles as

a function of the electrolyte from which the electrode was made. What is clear from the data in this table is that the presence of Mn^{2+} when the electrode is prepared, and ultimately the presence of a manganese oxide such as Mn_3O_4 or MnO_2 in the resultant electrode, leads to a significant enhancement in performance of the electrode.

3.4.3. EQCM Analysis

The mass of each of the electrodes was also monitored during the course of performance evaluation. Figure 12(a) compares the measured voltametric behaviour with the electrode mass during the course of a cycle, in this case the 50^{th} cycle for each electrode. Note that these are typical results for each of the electrodes. The first point to note is that the total mass change the each electrode undergoes is relatively small, being at most 15, 50 and 75 ng/cm^2 for the 0.001, 0.01 and 0.1 M deposition electrolytes, respectively.

During the course of the discharge-charge cycle it is apparent that for all of the electrodes the mass begins to increase when the main peak in cathodic current is obtained. This is interesting because the mass does not increase when this cathodic peak begins, but rather when the cathodic current maximum is achieved. This is also reflected by the hysteresis loop apparent in the mass versus charge data for the same electrodes, as shown in Figure 12(b). The maximum electrode mass is achieved when the reversal potential (1.0 V vs SCE) is reached. After this the mass decreases essentially back to its starting point, except in the case of the electrode made from 0.001 M Py + 0.001 M Mn^{2+}, in which case its mass was significantly lower than where it started. This may be evidence for the degradation of the composite electrode material. There is also evidence in the case of the electrode made from the 0.1 M Py + 0.1 M Mn^{2+} electrolyte of the electrode mass increasing about half way through the discharge half cycle (~0.5 V vs SCE). Based on previous EQCM studies [33], this is the result of manganese dioxide within the composite electrode.

The source of these mass changes arises from the electrochemical processes the components of the composite electrode undergo. When discharging (reducing) the cathode-active PPy, which is

a conducting polymer, we are essentially introducing an excess of negative charge into the polymer structure, which in itself is an interwoven array of individual polymer chains. While these chains do not form a monolithic structure, they do apparently make a very porous structure (cf. Figure 5) into which the electrolyte ions from the cycling electrolyte can permeate. As a result of this, under discharge the electrolyte cations are electrostatically attracted to the polymer surface, where they store charge and contribute to increasing the mass of the electrode. The manganese oxide formed in the composite electrode, if indeed it is MnO_2, undergoes discharge by intercalation, as has been reported in the studies on this material in the battery literature [34]; i.e.,

$$MnO_2 + M^+ + e^- \leftrightarrow MnOOM \qquad ...(11)$$

where in aqueous electrolytes, M^+ is mostly H^+, with other ions such as Li^+, Na^+ and K^+ also playing a role. This process is a redox reaction (enabling pseudo-capacitance), in which Mn(IV) is reduced to Mn(III) when M^+ and the electron are inserted into the manganese dioxide structure. Of course with the intercalation of foreign metal ions into the manganese dioxide structure, the electrode mass will also increase.

Figure 12(b) shows the rate of change of mass (m) with respect to charge (Q) data (dm/dQ) for selected regions of the voltametric data. For the electrodes prepared from the 0.1 and 0.01 M electrolytes there is very little mass change during the initial stages of discharge ($dm/dQ \approx 0$) suggesting the electrode is storing charge within the structure without the need for electrolyte ion association. At lower potentials there is clearly a mass increase at a rate of 592 μg/C (0.01 M) and 261 μg/C (0.1 M). In the electrolyte being used for cycling (0.1 M K_2SO_4) the addition of negative charge to the PPy should lead to K^+ ions electrostatically adsorbing onto the PPy surface at a theoretical rate of 405 μg/C. For the electrode made from 0.01 M Py + 0.01 M Mn^{2+} the higher experimental value indicates that other species are also associated with the adsorption. The hydration sheath around the K^+ ions is a likely source of added mass. The much lower dm/dQ value obtained for the electrode made from 0.1 M Py + 0.1 M Mn^{2+} indicates that not all of the composite electrodeposited material is being utilized during the cycling process. The electrode prepared from

0.001 M Py + 0.001 M Mn^{2+} exhibited behaviour that was quite different compared to those made from the other electrolytes. In particular, it showed considerable hysteresis with an electrode mass increase only becoming apparent after the reversal potential had been reached. Its value for dm/dQ was 229 μg/C, although caution is necessary interpreting this value given the differences in behaviour. As mentioned, all electrodes showed considerable hysteresis upon charge, with the mass change associated with the charge being extracted from the electrode always being less than the discharge; i.e., 155 μg/C (0.1 M), 226 μg/C (0.01 M) and 71 μg/C (0.001 M). This may result from the morphology (porosity) of the deposit inhibiting the removal of electrolyte ions, or alternatively that charge extraction from the discharged electrode is intrinsically more difficult than charge insertion into the uncharged electrode. Despite the hysteresis, the initial electrode mass was essentially recovered.

The mass changes that these composite electrodes undergo can be used to examine the charge efficiency; i.e., the amount of charge accommodated in the electrode as a function of the amount of material present. Figure 13 takes the mass changes the electrode undergoes during cycling (Figure 12(a)) and normalizes it based on the amount of active material present in the electrode. Here it becomes clear that the electrode made from 0.001 M Py + 0.001 M Mn^{2+} has the greatest utilization of its active material. This is most likely due to the morphology of the electrode, in which case the relatively low amount of material present, formed during the early stages of electrodeposition, presents the greatest surface area to the electrolyte, and hence results in the greatest mass uptake by the electrode. Such a heavy utilization may also be the cause of the loss in mass during cycling demonstrated by this electrode material.

3.4.4. EIS Analysis

EIS has been applied to the thin film electrodes to examine their properties and performance. In this case a sequence of 25 mV potential steps (with an intermediate rest time of 10 min) was applied to each electrode to cycle from the open circuit potential (0.30 V) to the upper anodic limit

(1.00 V), then to the lower cathodic limit (0.00 V), and then back up to the upper limit. This very slow cycling rate (equivalent to 0.042 mV/s) enables the characterization of the quasi-equilibrium nature of each electrode within the potential window being used. This approach also exacerbates any instability the electrode might experience during cycling that would otherwise only become apparent after an extended cycle life [32].

Figure 14(a) shows an example of the EIS data collected, in this case for the thin film electrode prepared from 0.001 M Py + 0.001 M Mn^{2+} in 0.1 M H_2SO_4. Each of the EIS data sets shows behaviour that is typical of a bounded porous electrode [35]. At high frequencies there is a linear region in the EIS data (inset in Figure 14(a)), which is the result of transport of the ionic electrolyte into the electrode pores, with a decreasing frequency leading to greater access of the pores by the electrolyte. As the frequency is decreased even further the electrode behaviour changes to indicate more conventional charge transfer and double layer processes at the porous electrode-electrolyte interface. The equivalent circuit used to model this EIS data is shown in Figure 14(b). The series resistance (R_s) takes into account the combined resistance of the thin film electrode and the electrolyte in the cell geometry being used. A constant phase element (CPE (D)) was then used to characterize mass transport (diffusion) of the electrolyte ions into the porous electrode. The impedance of a CPE (Z_{CPE}) is given by

$$Z_{CPE} = \frac{1}{T(j\omega)^P} \qquad ...(12)$$

where T is a composite value containing terms representing primarily the diffusion of electro-active species into the pores, j is the imaginary number, ω is the angular frequency, and P is a parameter indicating the divergence of the interface from ideal behaviour. P falls in the range 0-1, but ideal behaviour in this case is when P = 0.5, which is for a linear, non-tortuous pore. At lower frequencies the semicircular arc is typical of interfacial charge transfer and double layer behaviour at an electrified interface. As such we have accounted for this portion of the EIS data using a modified Randles circuit [36] that consists of the parallel arrangement of a charge transfer

resistance (R_{ct}) and a constant phase element (CPE (DL)) to represent the double layer capacitance of a rough and porous electrode-electrolyte interface. The charge transfer resistance essentially represents the kinetics of any charge transfer processes occurring at the electrode-electrolyte interface; i.e., Eqn (10), while the double layer capacitance represents the amount of charge stored at this interface. They are in a parallel arrangement because they are competing processes. The constant phase element used here is also defined by Eqn (12) above; however, in this case T represents the capacitance of the interface, while P again represents the divergence from a flat surface. For an ideal capacitor P = 1, which means that T = C. Typically for rough surfaces, P has a value greater that ~0.8. The double layer capacitance (C_{dl}) can be calculated from the CPE using the expression [28]

$$C_{dl} = T(\omega_{max})^{P-1} \quad ...(13)$$

where ω_{max} is the angular frequency when the imaginary impedance (-Z") is a maximum. To determine the optimum fitting parameters for the equivalent circuit to match the experimental data, complex non-linear least squares regression (CNLS), as defined by Boukamp, was used [37, 38]. A comparison of these fitting parameters for each of the electrodes prepared in this study is shown in Table 3.

The first comment to be made about the equivalent circuit fitting parameters is how they reflect on the reversibility of the thin film electrodes as a result of the potential step electrochemical cycling used here. The value of each of the reported parameters, but particularly C_{dl}, indicates that the as-prepared electrode exhibits the best performance, but after cycling the performance degrades to an approximately steady state value that is dependent on the potential. Certainly this observation is consistent with the extended cycling shown in Figure 11, where the specific capacitance fades with cycling to an approximately constant value.

The series resistance (R_s) incorporated in the model compensates for the resistance of both the electrolyte and electrode. Now given the relatively large volume of electrolyte used in these experiments, changes in the electrolyte resistance are expected to be negligible, and so any changes

observed in R_s likely reflect the behaviour of the thin polymer film. As an aside, it is difficult to compare R_s for different electrodes because its value is dependent on the geometry of the electrochemical cell used and our ability to reproducibly place the working and reference electrodes in exactly the same place for every experiment. While the values of R_s were similar across the experiments considered, the differences were most likely due to irreproducibility in the placement of the electrodes rather than any changes in the electrode. However, for an individual electrode, changes in R_s represent changes in the resistance of the electrode, since, as mentioned above, the electrolyte contribution for an individual electrode should remain the same. Therefore, for each electrode, what was noted was the relatively low value of R_s for the initially prepared electrode at the open circuit potential (0.30 V vs SCE). Upon oxidation to 1.00 V R_s increased, but upon reduction the value of R_s decreased, the relative magnitude of which was found to depend on the amount of polymer present; i.e., the relative changes in R_s were the smallest for the thin electrodes prepared from the dilute electrolytes, compared to the thicker electrodes prepared from the more concentrated electrolytes. Certainly this was to be expected given the dependence of R_s (Ω) on the resistivity (Ω cm) and thickness of the film.

The charge transfer resistance data extracted from the fitting provides an indication of the kinetics of electron injection and extraction into and out of the PPy structure. For all of the electrodes studies, R_{ct} was on average quite large indicating the difficulty associated with PPy solid state redox processes. It is important to recognize that R_{ct} is also an area specific term, which means that it is dependent on both the intrinsic charge transfer resistance (i.e., Ω cm), as well as the area over which that charge transfer takes place. For each of the individual electrodes the trend in R_{ct} with applied potential was similar to that of R_s, indicating that it is intrinsically easier to insert charge into the PPy structure at lower potentials, or that the electrode morphology is changing so as to lower the electrode-electrolyte interfacial area. The magnitude of these changes in R_{ct} with applied potential would indicate that these effects are quite dramatic.

Perhaps what is of most importance in discussing these PPy films are the changes in double

layer capacitance (C_{dl}), which is again an area specific term. For an individual electrode the changes in C_{dl} are closely related to R_{ct}, which was expected since they are competing parallel processes for charge storage within the electrode. For instance, a high value for R_{ct} indicates that little charge is stored via faradaic processes, with the majority instead being stored in the double layer. For all of the electrodes the value of C_{dl} was considerably higher for the fresh uncycled electrode at the open circuit potential. Then upon cycling it was noted that C_{dl} was most often higher at the anodic limit. The likely cause for this is the relatively higher resistance of the thin film electrode, as indicated by R_s, meaning that more charge is to be found at the interface contributing to double layer storage, rather than to bulk faradaic processes. It was also noted that C_{dl} decreased with cycling, which is consistent with the decrease in specific capacitance shown in Figure 11. The cause of this is not known with certainty, but is likely due to an irreversible change in the morphology of the electrode film leading to a lower interfacial area. This effect was exacerbated with the use of thicker electrodes which showed much higher initial values for C_{dl} that dropped to values that are essentially the same irrespective of the electrode thickness. The implication is that the thinner electrodes achieve a greater utilization of the active material during cycling, whereas the thicker electrodes only utilize the near-surface region after the bulk of the electro-active material is isolated during the initial part of cycling. This is consistent with the charge efficiency data in Figure 13.

4. SUMMARY AND CONCLUSIONS

In this work the properties and performance of composite Mn-modified PPy electrodes prepared by electrodeposition has been evaluated and compared to PPy-only electrodes. The following key points have been derived:

(i) The composite Mn-modified PPy electrodes exhibited a considerably enhanced performance as supercapacitor electrode materials compared to PPy-only electrodes prepared in a similar fashion.

(ii) The origin of this enhanced performance stems partially from the morphology of the electrodeposited films, which showed an increase in electrochemically active surface area of up to 30 times greater than the substrate.

(iii) It also stems from the specific capacitance of the manganese oxide incorporated into the composite, which has in previous reports from our group shown to be quite high using a similar approach.

(iv) Quantification of this increase in electrode surface area was carried out using a novel approach based on the modelling of chronoamperometric electrodeposition data using multiple applications of the Cottrell equation. This modelling was based on the mechanism of PPy electrodeposition, which at very short times involved the diffusion limited transport of Py to the bare platinum substrate, followed at longer times by diffusion limited transport of Py to a higher area PPy-coated substrate. The electrode area increased proportionately with the concentration of the Py in the electrolyte.

(v) Morphological analysis of the Mn-modified PPy films by AFM and profilometry has shown that both thicker and rougher films result from electrodeposition from more concentrated electrolytes. TEM has also shown that the Mn-modification leads to the formation of nano-scale manganese oxide crystallites within the PPy film.

(vi) Electrochemically thinner films of Mn-modified PPy exhibit excellent performance, with specific capacitances of over 2000 F/g being reported. This was deduced to be due to greater utilization of the thinner films.

5. ACKNOWLEDGEMENTS

The authors acknowledge Dr. Monica Rossignoli for her assistance in collecting the ICP-OES data, Dr. Glenn Bryant for his assistance in collecting the AFM images, and Dr. Victor Wong for his assistance in obtaining the TEM images. PN also acknowledges the financial support provided by DIKTI in terms of a scholarship.

6. REFERENCES

[1] S. de la Rue du Can; 'Global Energy Sources and Trends' in *Encyclopedia of Environmental Health*, Ed. J. O. Nriagu, Elsevier, Vol. 2, pp. 987-994.

[2] D. Ragone; Proc. Soc. Automotive Engineers Conference, Detroit, MI, USA (1968).

[3] R. H. Crabtree; *Energy Production and Storage: Inorganic Chemical Strategies for a Warming World*, John Wiley and Sons (2010).

[4] A. Burke; *J. Power Sources*, 91 (2000) 37-50.

[5] D. Zhang, X. Zhang, Y. Chen, C. Wang, Y. Ma, H. Dong, L. Jiang, Q. Meng and W. Hu; *Phys. Chem. Chem. Phys*, 14 (2012) 10899-10903.

[6] E. Frackowiak and F. Beguin; *Carbon*, 40 (2002) 1775-1787.

[7] R. Kotz and M. Carlen; *Electrochim. Acta*, 45 (2000) 2483-2498.

[8] P. Simon and Y. Gogotsi; *Nat. Mater*., 7 (2008) 845-854.

[9] V. V. N. Obreja, *Physica E: Low-Dimensional Systems and Nanostructures*, 40 (2008) 2596-2605.

[10] M. J. Bleda-Martínez, J. A. Maciá-Agulló, D. Lozano-Castelló, E. Morallón, D. Cazorla-Amorós, A. Linares-Solano; *Carbon*, 43 (2005) 2677-2684.

[11] B. E. Conway; *Electrochemical Supercapacitors: Scientific Fundamentals and Technological Applications*, Kluwer Academic, New York (1999).

[12] C. Peng, S. Zhang, D. Jewell and G. Z. Chen; *Progress in Natural Science*, 18 (2008) 777-788.

[13] K. Naoi and P. Simon; *Electrochemical Society Interface*, 17 (2008) 34-37.

[14] K. Gurunathan, A.Vadivel Murugan, R. Marimuthu, U. P Mulik and D.P. Amalnerkar; *Materials Chemistry and Physics*, 61 (1999) 173-191.

[15] A. Rudge, I. Raistrick, S. Gottesfeld and J. P. Ferraris; *Electrochim. Acta*, 39 (1994) 273-287.

[16] E. Frackowiak, V. Khomenko, K. Jurewicz, K. Lota and F. Béguin; *J. Power Sources*, 153 (2006) 413-418.

[17] J. R. Miller and P. Simon; *Science*, 321 (2008) 651-652.

[18] I. H. Kim, J. H. Kim, Y. H. Lee and K. B. Kim; *J. Electrochem. Soc.*, 152 (2005) A2170-A2178.

[19] A. Cross, A. Morel, A. Cormie, A. F. Hollenkamp and S. W. Donne; *J. Power Sources*, 196 (2011) 7847-7853.

[20] M. T. Lee, J. K. Chang, Y. T. Hsieh, W. T. Tsai and C. W. Lin; *J. Solid State Electrochem.*, 14, (2010) 1697-1703.

[21] B. Babakhani and D. G. Ivey; *J. Power Sources*, 195 (2010) 2110-2117.

[22] F. Moser, L. Athouel, O. Crosnier, F. Favier, D. Belanger and T. Brousse; *Electrochem. Comm.*, 11 (2009) 1259-1261.

[23] S. R. Sivakkumar, J. M. Ko, D. Y. Kim, B. C. Kim and G. G. Wallace, *Electrochim. Acta*, 52 (2007) 7377-7385.

[24] Z. H. Dong, Y. L. Wei, W. Shi and G. A. Zhang, *Mat. Chem. Phys.*, 131 (2011) 529-534.

[25] R. K. Sharma, A. C. Rastogi, S. B. Desu; *Electrochim. Acta*, 53 (2008) 7690-7695.

[26] B. R. Scharifker, E. Garcia-Pastoriza and W. Marino; *J. Electroanal. Chem. Interfac. Electrochem.*, 300 (1991) 85-98.

[27] L. F. Q. P. Marchesi, F. R. Simoes, L. A. Pocrifka and E. C. Pereira; *J. Phys. Chem. B*, 115 (2011) 9570-5.

[28] A. J. Bard and L. R. Faulkner; *Electrochemical Methods: Fundamentals and Applications*, Wiley (2000).

[29] M. Fleischmann and H. R. Thirsk; *Electrochim. Acta*, 1 (1959) 146.

[30] P. Saville; *Polypyrrole: Formation and Uses*, Defence R&D Canada, Technical Memo (2005).

[31] G. Aylward and T. Findlay; *SI Chemical Data, 6th Edition*, John Wiley and Sons, Australia (2008).

[32] A. Cormie, A. D. Cross, A. F. Hollenkamp and S. W. Donne; *Electrochim. Acta*, 55, (2010) 7470-7478.

[33] A. D. Cross, I. Oclomendy, M. Drozd, A.F. Hollenkamp and S. W. Donne; *J. Electrochem. Soc.*160, (2013) A368-A375.

[34] S. W. Donne, G. A. Lawrance and D. A. J. Swinkels; *J. Electrochem. Soc.*, 144 (1997) 2949.

[35] R. De Levie; *Adv. Electrochem. Electrochem. Eng.*, 6 (1967) 329.

[36] J. E. B. Randles; Disc. Faraday Soc., 1 (1947) 11.

[37] B.A. Boukamp, Solid State Ionics, 18, 136 (1986).

[38] B.A. Boukamp, Solid State Ionics, 20, 30 (1986).

Table 1. Properties of the PPy and Mn-modified PPy films. Chronoamperometric step potential = 0.75 V vs SCE, step time = 30 s, and 0.1 M H_2SO_4 as the supporting electrolyte.

Electrolyte		EQCM Mass	Charge	Relative Area	[Mn][a]	dm/dQ	Capacitance[b]
[Py] (M)	[Mn^{2+}] (M)	($\mu g/cm^2$)	(C/cm^2)	Increase	($\mu g/cm^2$)	($\mu g/C$)	(F/g)
0.001	0	1.1±0.6	2.1×10^{-3}	8.8	-	383	892
0.001	0.001	0.7±0.1	8.0×10^{-4}	3.9	0.17±0.05	943	2213
0.01	0	12±2	0.036	19.6	-	302	72
0.01	0.01	8±1	0.027	19.6	1.7±0.2	290	139
0.1	0	33±4	0.092	32.5	-	334	45
0.1	0.1	26±1	0.079	30.2	14.3±1.9	323	60

[a] Employed ICP-OES

[b] Electrodes were cycled in 0.1 M K_2SO_4 between 0.0-1.0 V versus SCE at a rate of 5 mV/s.

Table 2. Roughness and thickness data for the composite electrode materials.

[Py] (M)	[Mn^{2+}] (M)	RMS Roughness (nm)	Thickness (nm)	Density (g/cm^3)
0.001	0.001	5.2±0.5	NA	NA
0.01	0.01	7.4±0.5	50±12	2.00
0.1	0.1	8.6±0.5	183±21	1.91

Table 3. Equivalent circuit parameters.

Electrolyte		Potential	R_s	CPE (Mass Transport)		R_{ct}	CPE (Capacitance)		C_{dl}
[Py] (M)	[Mn^{2+}] (M)	(V vs SCE)	(Ω)	T ($\times 10^3$)	P	(Ω)	T ($\times 10^4$)	P	(μF)
0.001	0	0.30	18.95	8.21	0.396	148400	1.99	0.882	313
		1.00 (A)	19.01	10.65	0.378	31273	2.01	0.880	258
		0.00 (C)	18.80	2.81	0.510	8112	1.94	0.932	200
		1.00 (A)	18.68	6.58	0.437	23042	2.03	0.905	238
0.001	0.001	0.30	16.32	16.49	0.341	11331	3.11	0.942	336
		1.00 (A)	16.16	13.98	0.326	8628	1.86	0.966	189
		0.00 (C)	15.77	17.73	0.309	5985	2.11	0.937	214
		1.00 (A)	15.55	14.15	0.319	10573	1.80	0.967	184
0.01	0	0.30							
		1.00 (A)							
		0.00 (C)	17.27	1.04	0.607	7311	2.20	0.978	218
		1.00 (A)							
0.01	0.01	0.30	6.82	11.91	0.146	63428	2.82	0.836	496
		1.00 (A)	18.42	21.91	0.325	83742	1.93	0.842	325
		0.00 (C)	16.97	2.28	0.524	7493	2.02	0.944	207
		1.00 (A)	17.51	5.33	0.489	21145	2.07	0.897	246
0.1	0	0.30	18.28	23.48	0.291	1114	11.08	0.703	1212
		1.00 (A)							
		0.00 (C)	20.07	1.05	0.592	7614	2.21	0.984	220
		1.00 (A)	22.72	1.39	0.606	18225	2.39	0.943	261
0.1	0.1	0.30	17.89	2.54	0.520	1330	13.73	0.693	1792
		1.00 (A)	21.63	5.89	0.416	22855	1.67	0.861	208
		0.00 (C)	18.59	1.33	0.580	6132	1.92	0.950	194
		1.00 (A)	20.32	3.65	0.507	20981	2.03	0.896	240

Table and Figure Captions

Figure 1. Linear sweep voltammetry data collected on the 0.1 M Py + 0.1 M Mn^{2+} (0.1 M H_2SO_4) electrolyte. Platinum substrate; scan rate = 5 mV/s.

Figure 2. Mechanistic pathways for the electrodeposition of manganese dioxide.

Figure 3. Chronoamperometric data for each of the Py + Mn^{2+} electrolytes considered in this study. Platinum substrate; step potential = 0.75 V vs SCE.

Figure 4. Fitting of the Cottrell equation to the early stages of the experimental chronoamperometric i-t data for the 0.001 Py + 0.001 M Mn^{2+} (0.1 M H_2SO_4) electrolyte. Platinum substrate; step potential = 0.75 V vs SCE. Inset: $i\text{-}t^{-1/2}$ for the same data set.

Figure 5. Relative area change for each for each of the thin electrode films prepared in this study.

Figure 6. Chronoamperometric and massogram data collected during electrodeposition from the 0.01 M Py + 0.01 M Mn^{2+} (0.1 M H_2SO_4) electrolyte. Platinum substrate; step potential = 0.75 V vs SCE.

Figure 7. Transmission electron micrograph of a Mn-modified PPy composite electrode prepared from the 0.1 M Py + 0.1 M Mn^{2+} (0.1 M H_2SO_4) electrolyte, with the dark regions indicating crystallites of manganese oxide.

Figure 8. Typical AFM images of the films prepared in this work. Note the vertical scale in each of the images.

Figure 9. Relative Mn-modified PPy electrode area increase as a function of the concentration of electroactive species in the electrolyte. Inset: Evidence for this as a logarithmic relationship.

Figure 10. Cyclic voltammetry data comparing the behaviour of the Mn-modified PPy (solid line) and PPy-only (dashed line) electrode films for each concentration of Py (+ Mn^{2+}) used in this study. Platinum substrate; 0.1 M K_2SO_4 electrolyte; scan rate = 5 mV/s.

Figure 11. Cycle stability of the thin electrode films prepared in this study. Platinum substrate; 0.1 M K_2SO_4 electrolyte; scan rate = 5 mV/s. Inset: Comparison in specific capacitance between the electrodes prepared from 0.001 M Py + 0.001 M Mn^{2+} (solid squares) and 0.001 M Py (open squares).

Figure 12. (a) Comparison between the cyclic voltammetry and EQCM massogram data for each of the thin electrode films prepared in this work. (b) Mass versus charge data for the same electrodes. Platinum substrate; 0.1 M K_2SO_4 electrolyte; scan rate = 5 mV/s; data from the 50^{th} cycle.

Figure 13. Charge efficiency, expressed as the ratio between the electrode mass change and the starting mass, for each of the thin film electrodes prepared in this work.

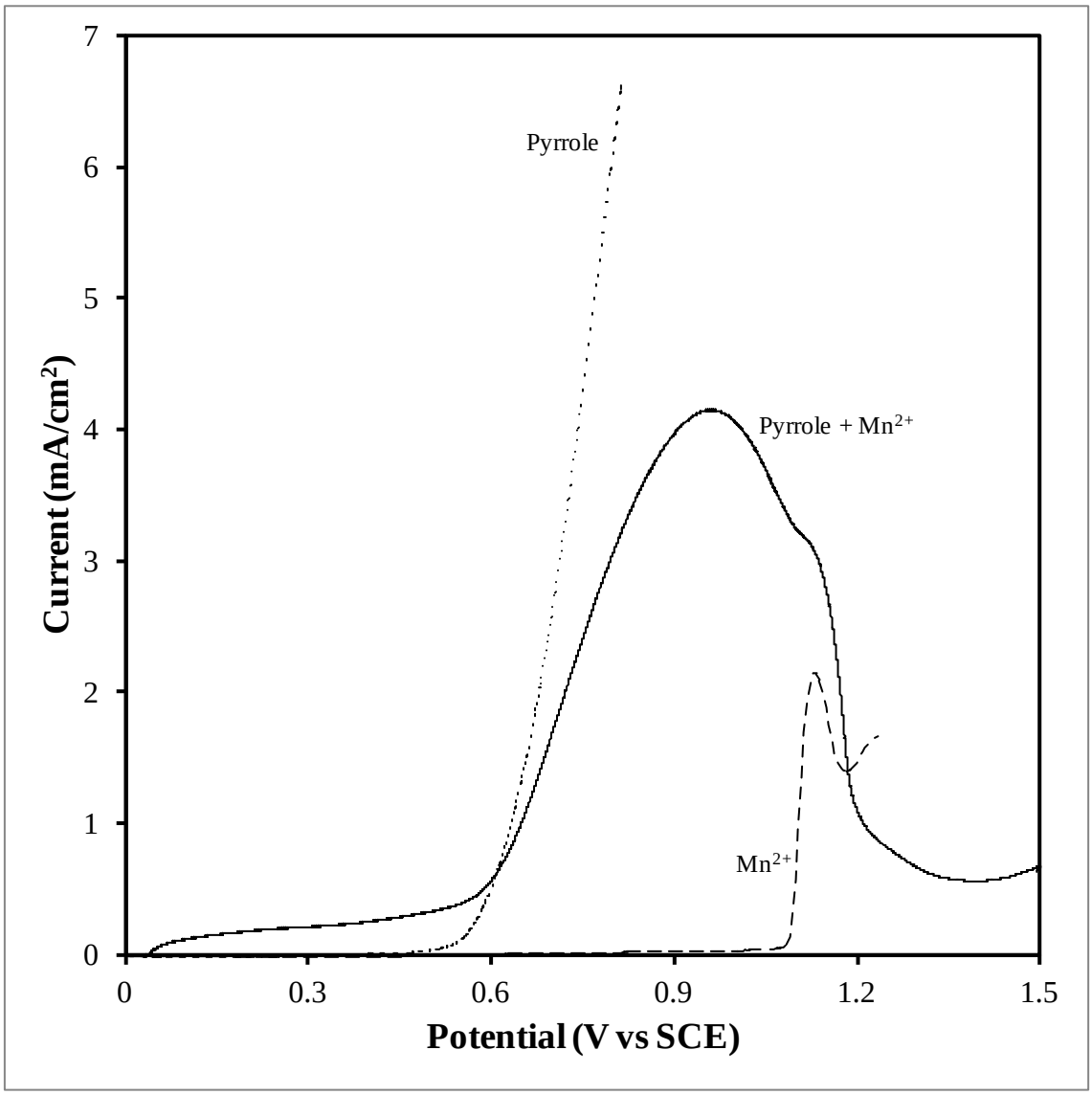

Figure 1. Linear sweep voltammetry data collected on the 0.1 M Py + 0.1 M Mn^{2+} (0.1 M H_2SO_4) electrolyte. Platinum substrate; scan rate = 5 mV/s.

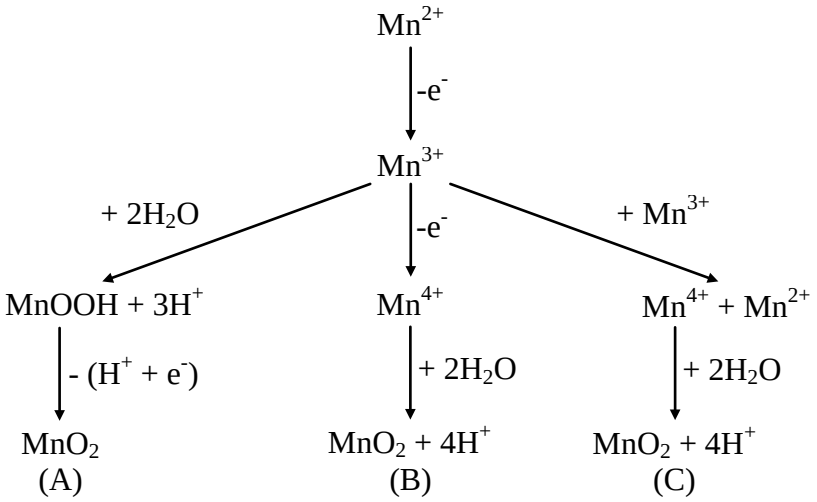

Figure 2. Mechanistic pathways for the electrodeposition of manganese dioxide.

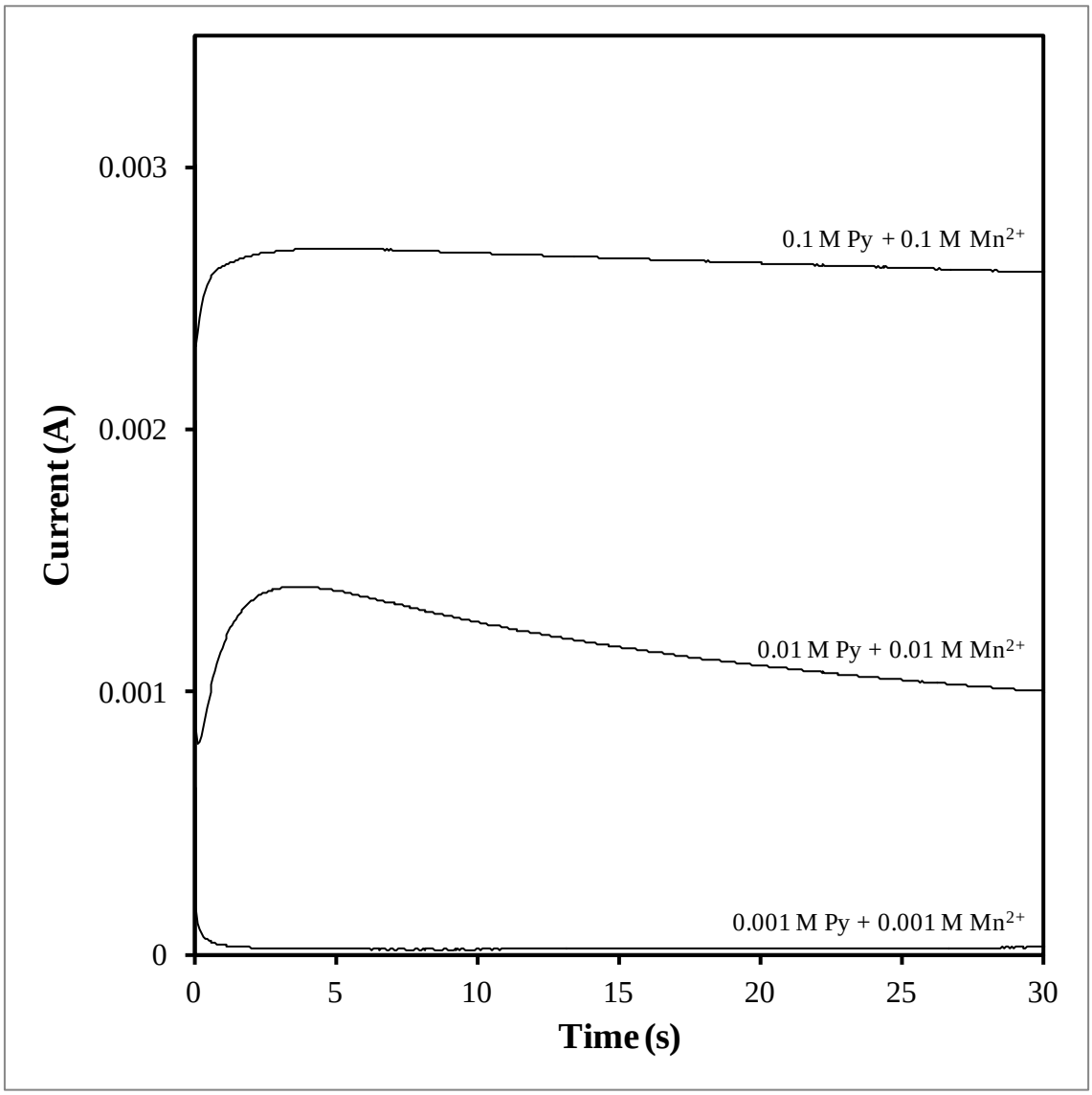

Figure 3. Chronoamperometric data for each of the Py + Mn^{2+} electrolytes considered in this study. Platinum substrate; step potential = 0.75 V vs SCE.

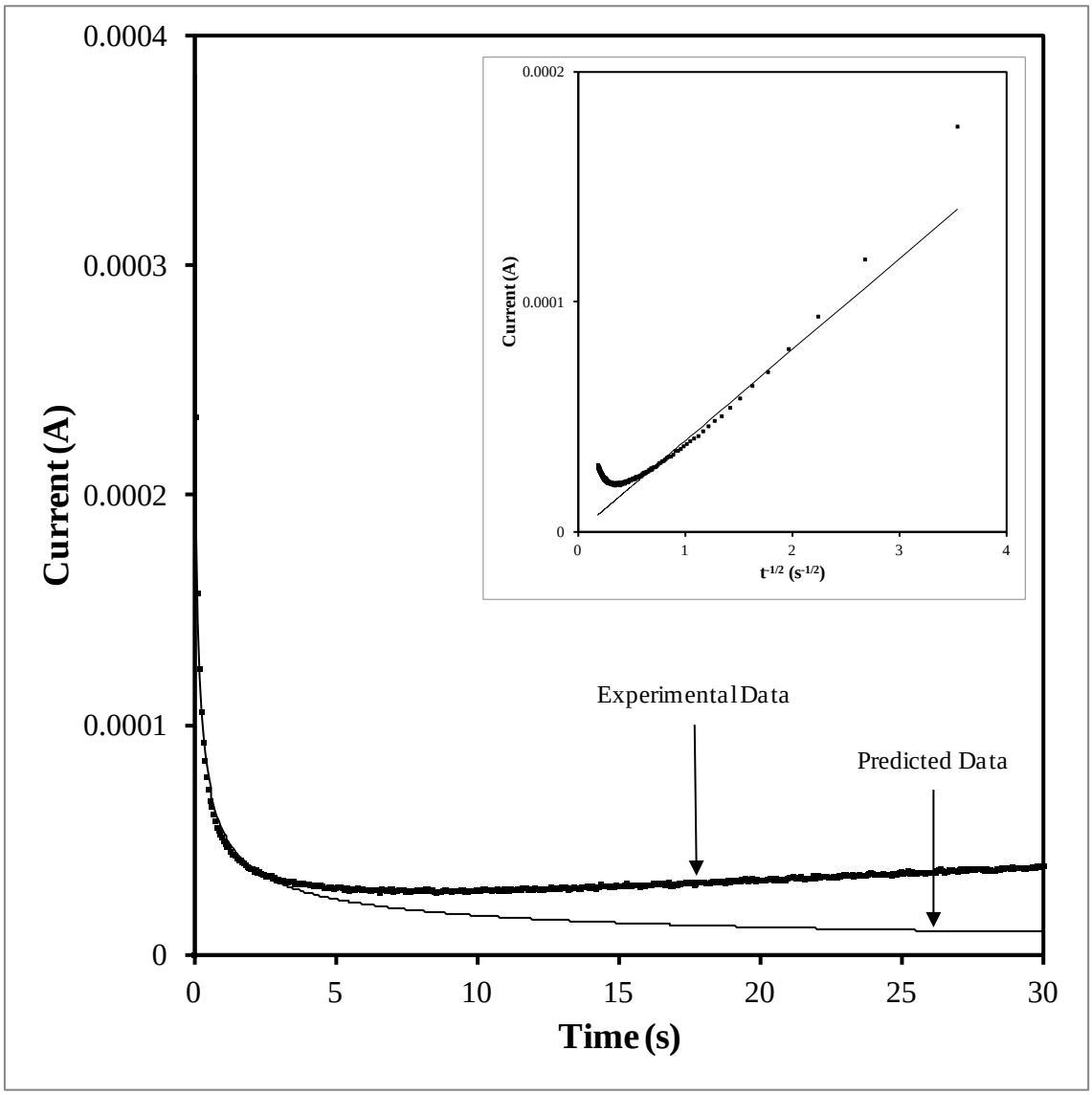

Figure 4. Fitting of the Cottrell equation to the early stages of the experimental chronoamperometric i-t data for the 0.001 Py + 0.001 M Mn^{2+} (0.1 M H_2SO_4) electrolyte. Platinum substrate; step potential = 0.75 V vs SCE. Inset: i-$t^{-1/2}$ for the same data set.

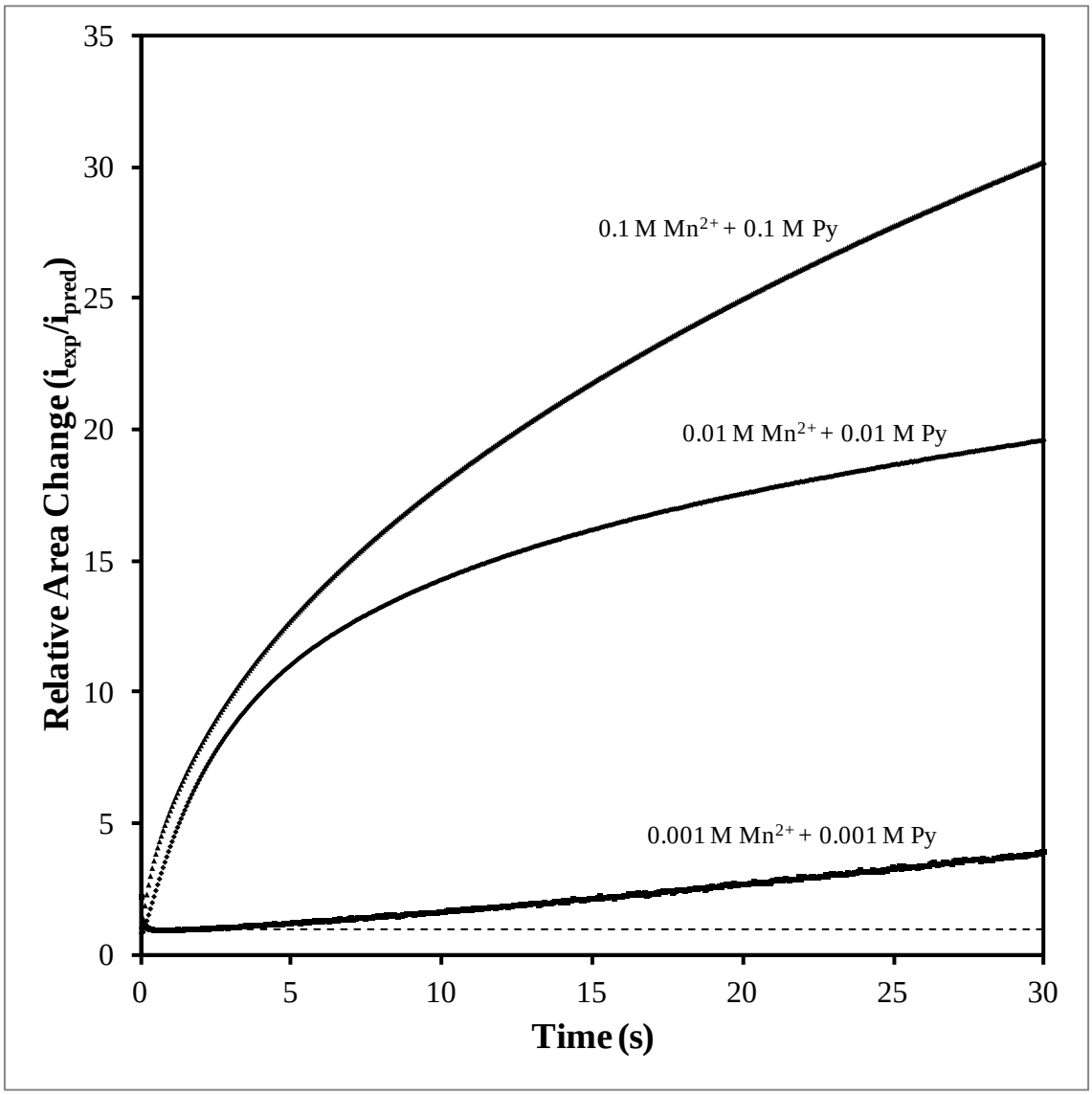

Figure 5. Relative area change for each for each of the thin electrode films prepared in this study.

(a)

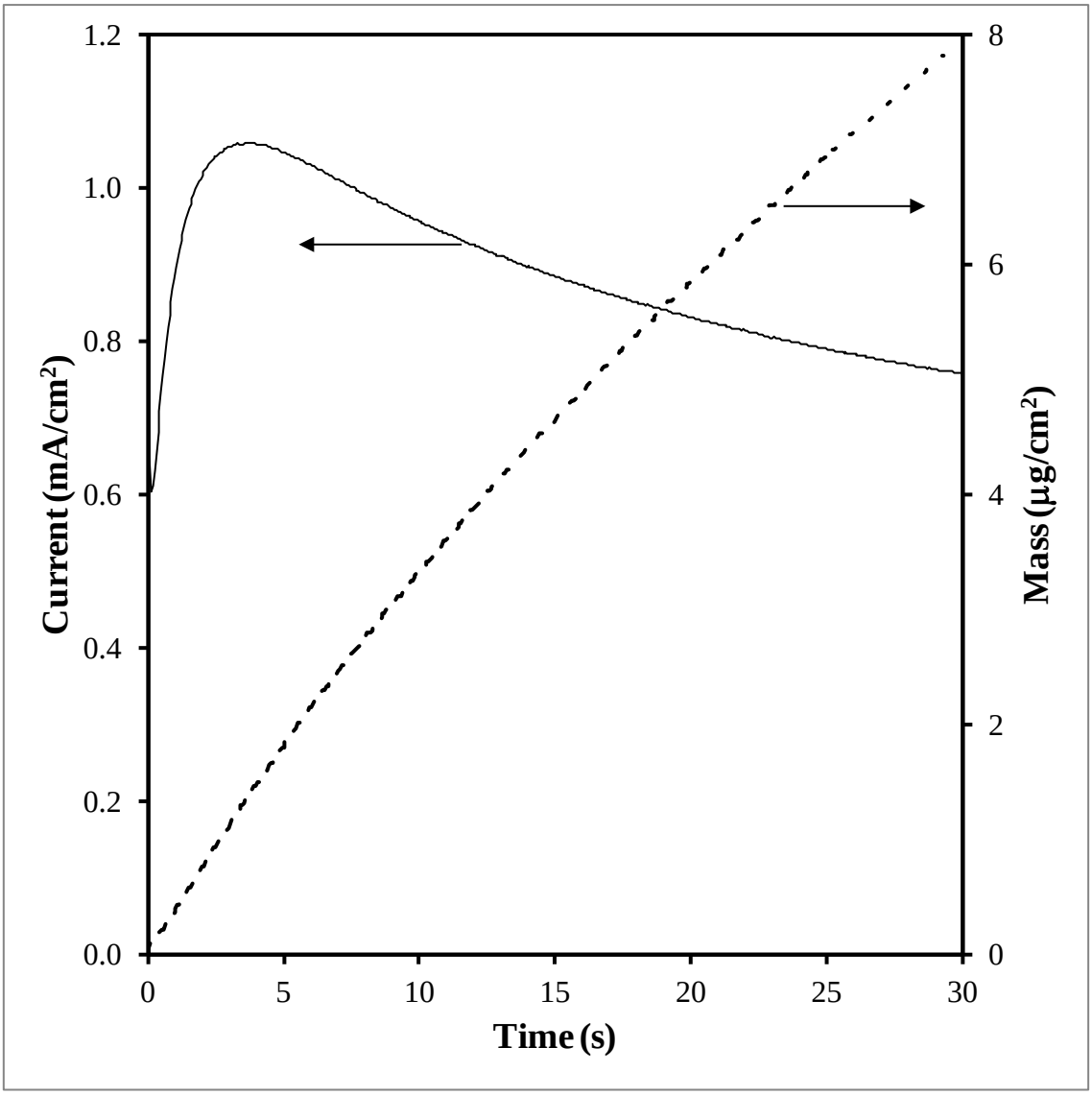
1.2
1.0
0.8
0.6
0.4
0.2
0.0
Current (mA/cm²)
8
6
4
2
0
Mass (µg/cm²)
0
5
10
15
20
25
30
Time (s)

(b)

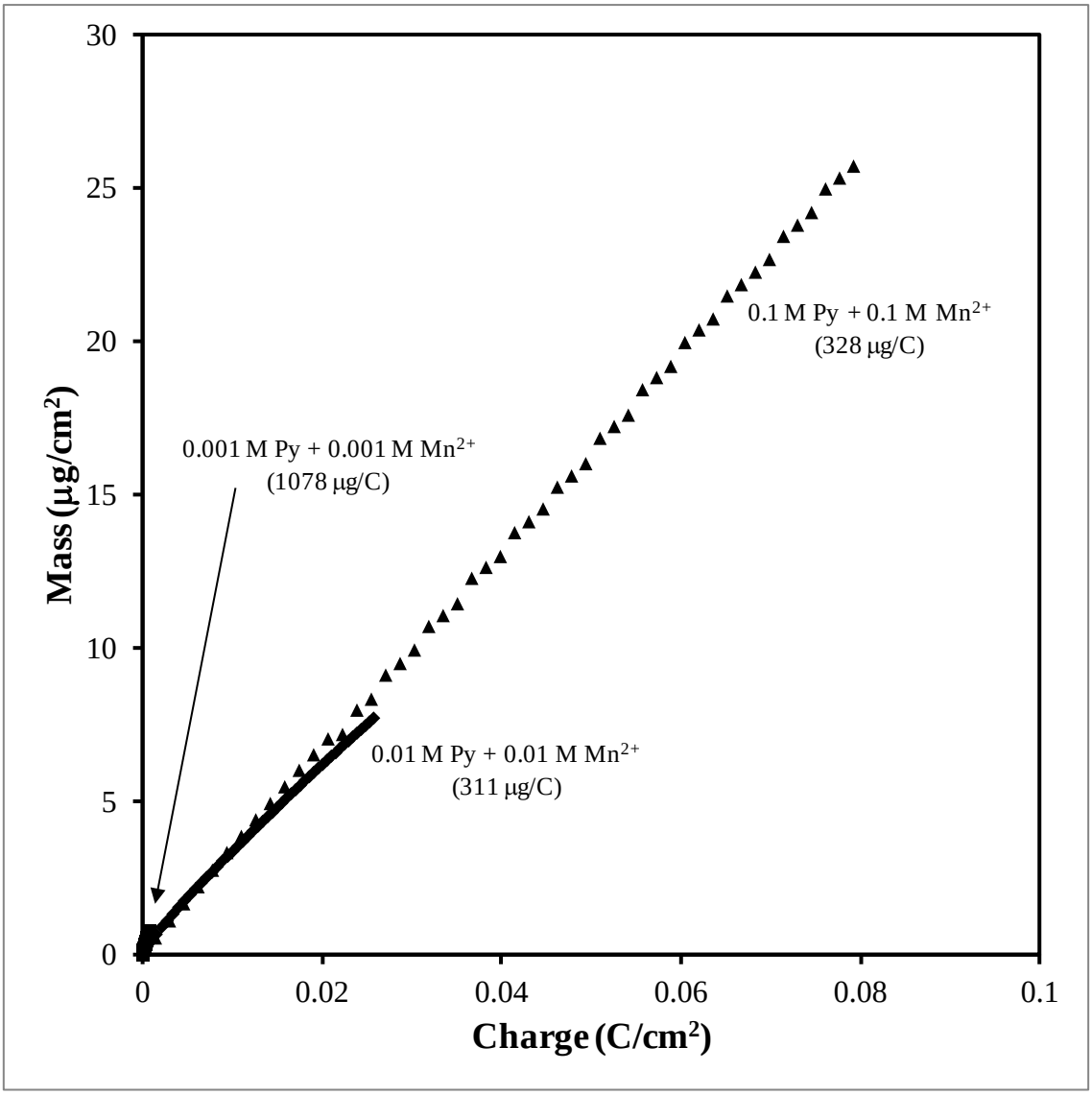

Figure 6. (a) Chronoamperometric and massogram data collected during electrodeposition from the 0.01 M Py + 0.01 M Mn^{2+} (0.1 M H_2SO_4) electrolyte. (b) EQCM and chronoamperometric data conversion to a plot of mass versus charge passed for the Mn^{2+} containing solutions considered. Platinum substrate; step potential = 0.75 V vs SCE.

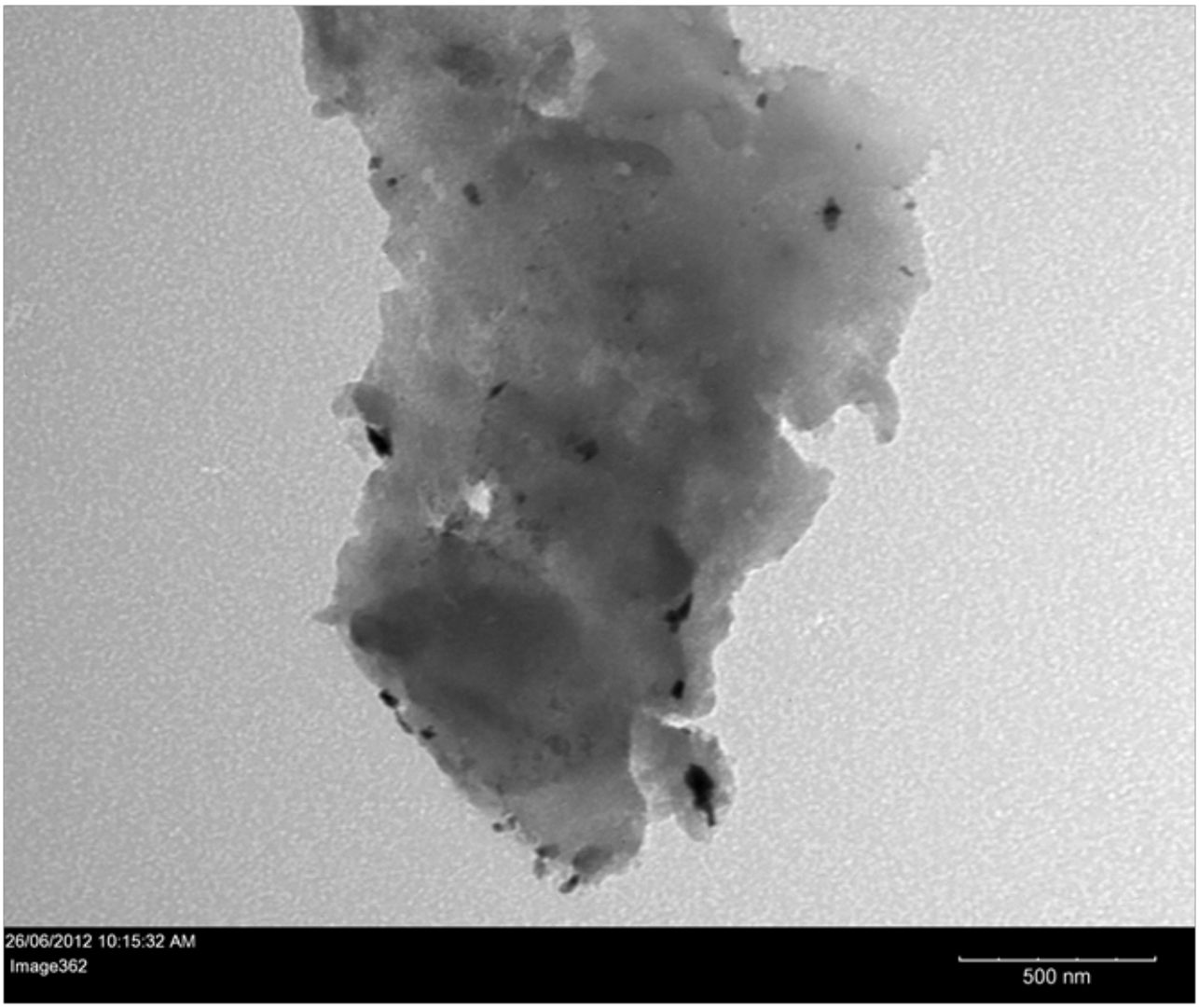

Figure 7. Transmission electron micrograph of a Mn-modified PPy composite electrode prepared from the 0.1 M Py + 0.1 M Mn^{2+} (0.1 M H_2SO_4) electrolyte, with the dark regions indicating crystallites of manganese oxide.

(a) 0.001 M Py + 0.001 M Mn^{2+}

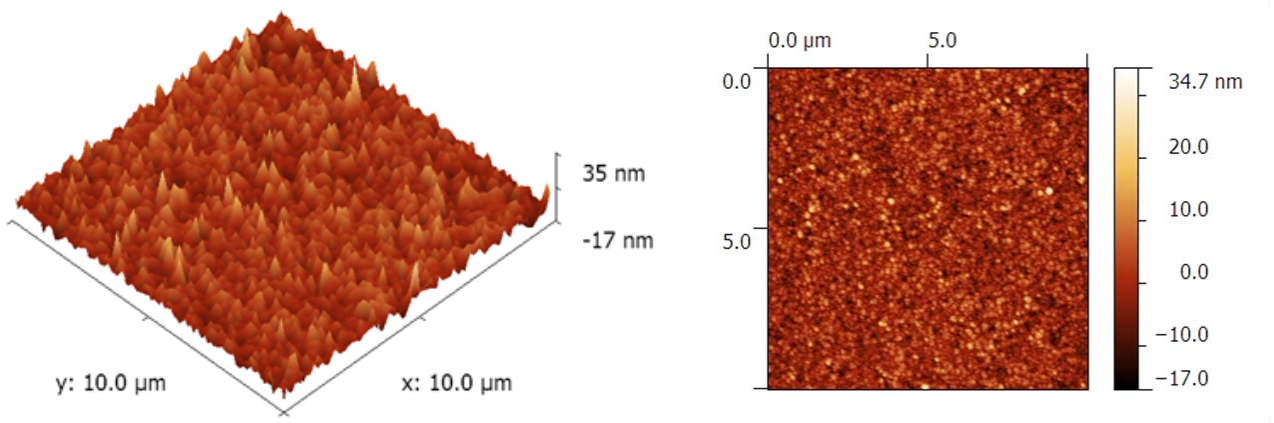

(b) 0.01 M Py + 0.01 M Mn^{2+}

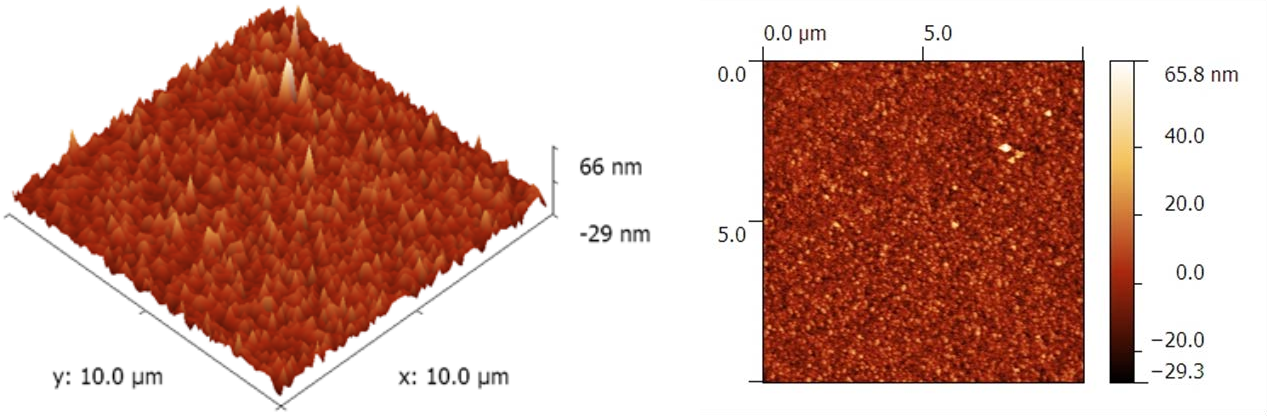

(c) 0.1 M Py + 0.1 M Mn^{2+}

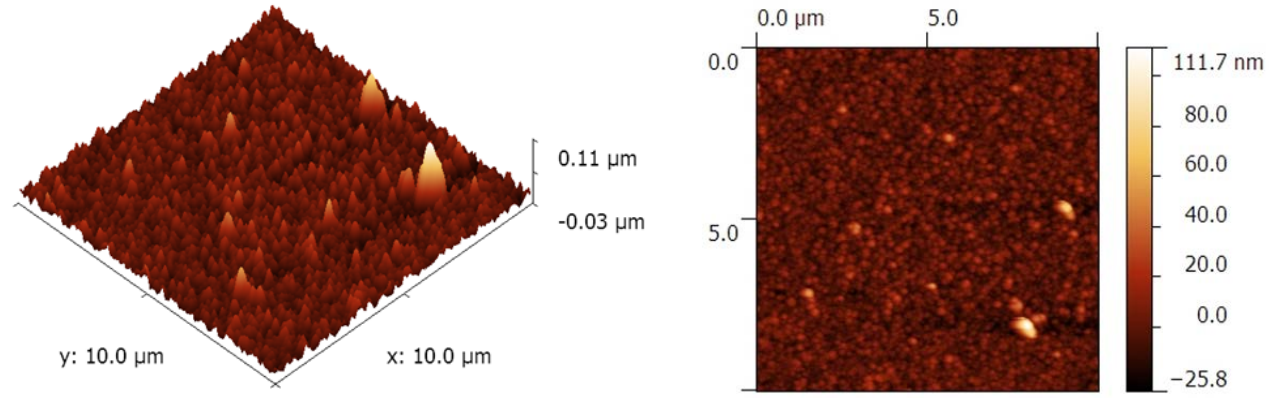

Figure 8. Typical AFM images of the films prepared in this work. Note the vertical scale in each of the images.

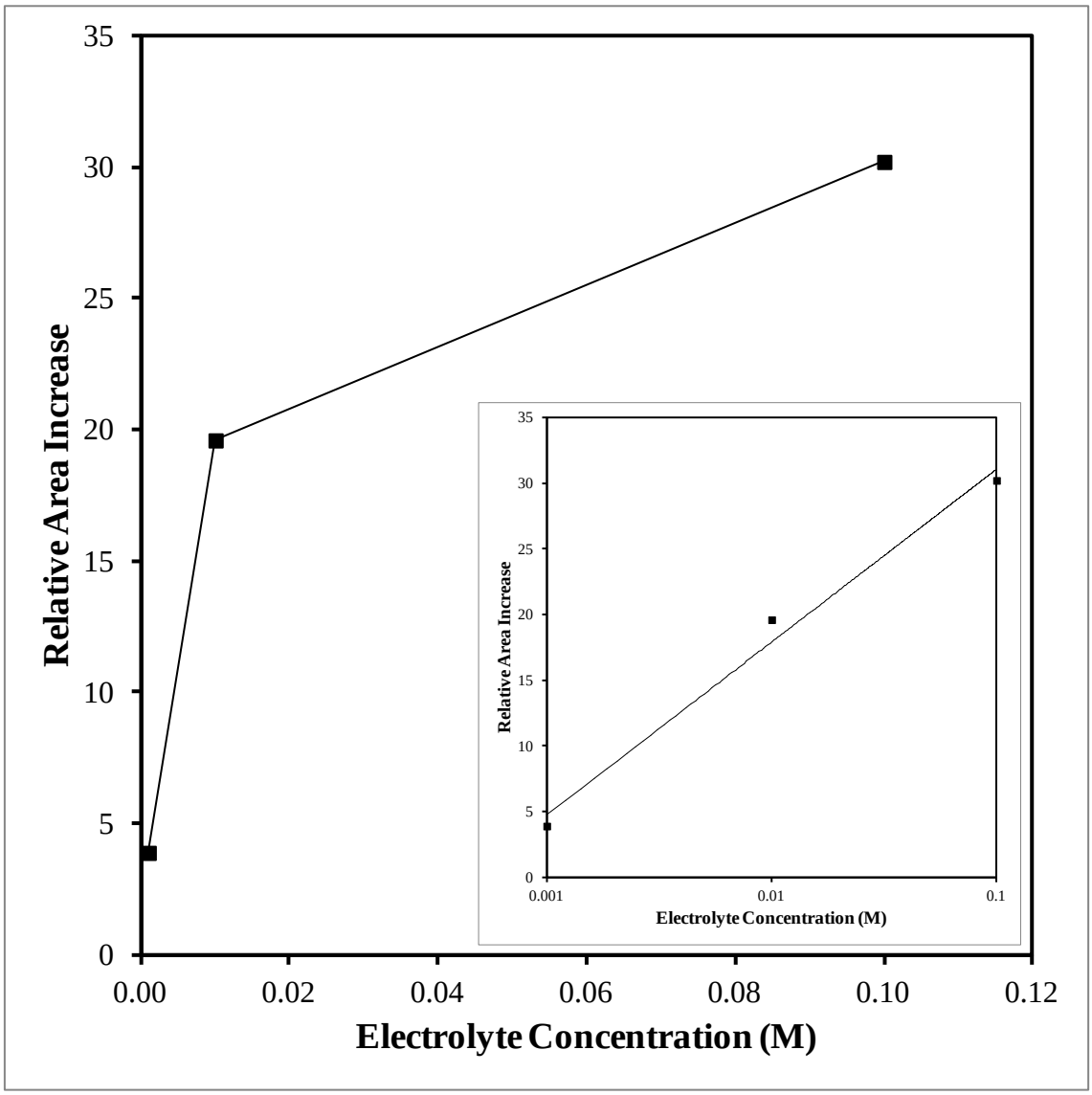

Figure 9. Relative Mn-modified PPy electrode area increase as a function of the concentration of electroactive species in the electrolyte. Inset: Evidence for this as a logarithmic relationship.

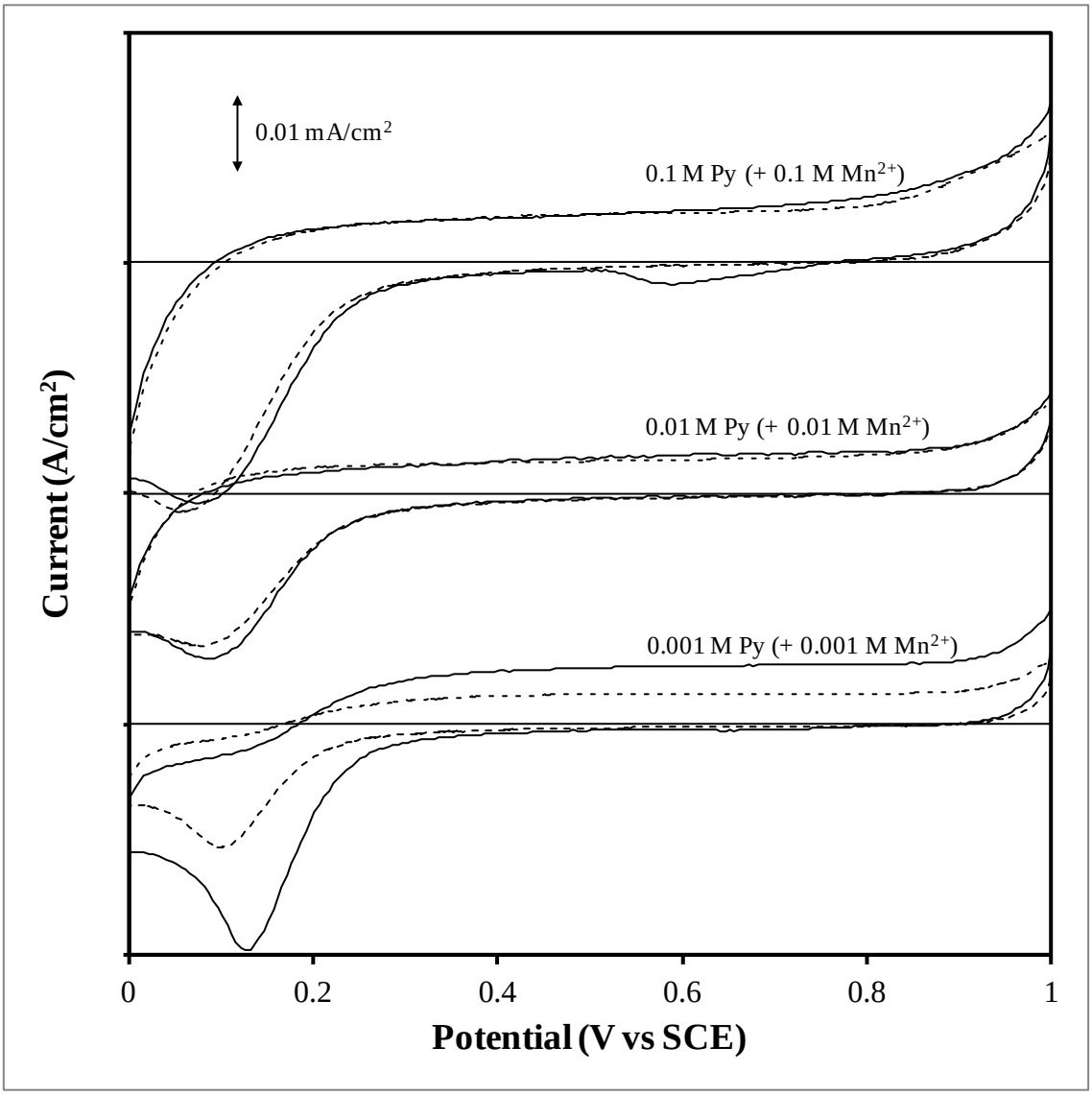

Figure 10. Cyclic voltammetry data comparing the behaviour of the Mn-modified PPy (solid line) and PPy-only (dashed line) electrode films for each concentration of Py (+ Mn^{2+}) used in this study. Platinum substrate; 0.1 M K_2SO_4 electrolyte; scan rate = 5 mV/s.

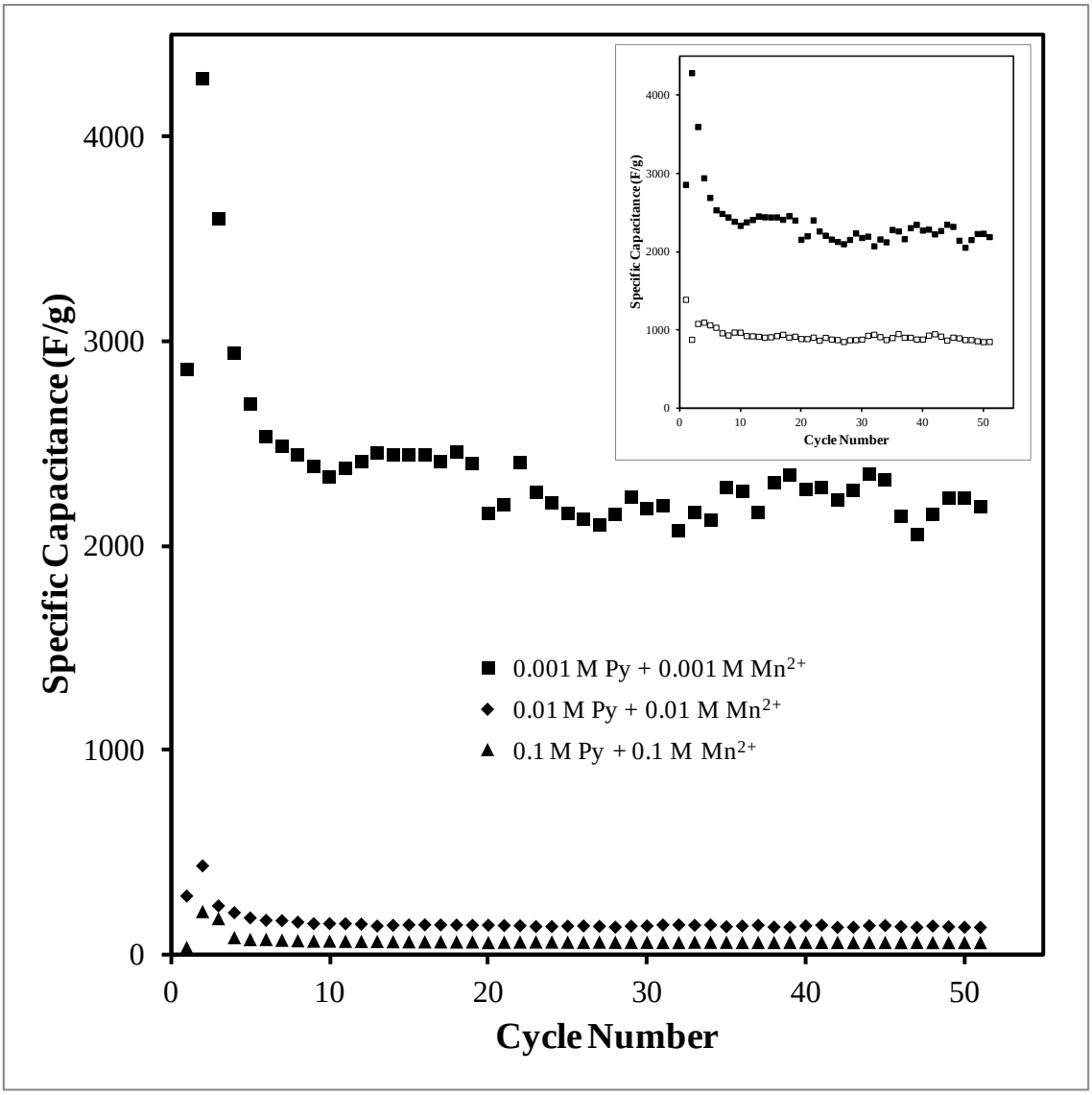

Figure 11. Cycle stability of the thin electrode films prepared in this study. Platinum substrate; 0.1 M K_2SO_4 electrolyte; scan rate = 5 mV/s. Inset: Comparison in specific capacitance between the electrodes prepared from 0.001 M Py + 0.001 M Mn^{2+} (solid squares) and 0.001 M Py (open squares).

(a)

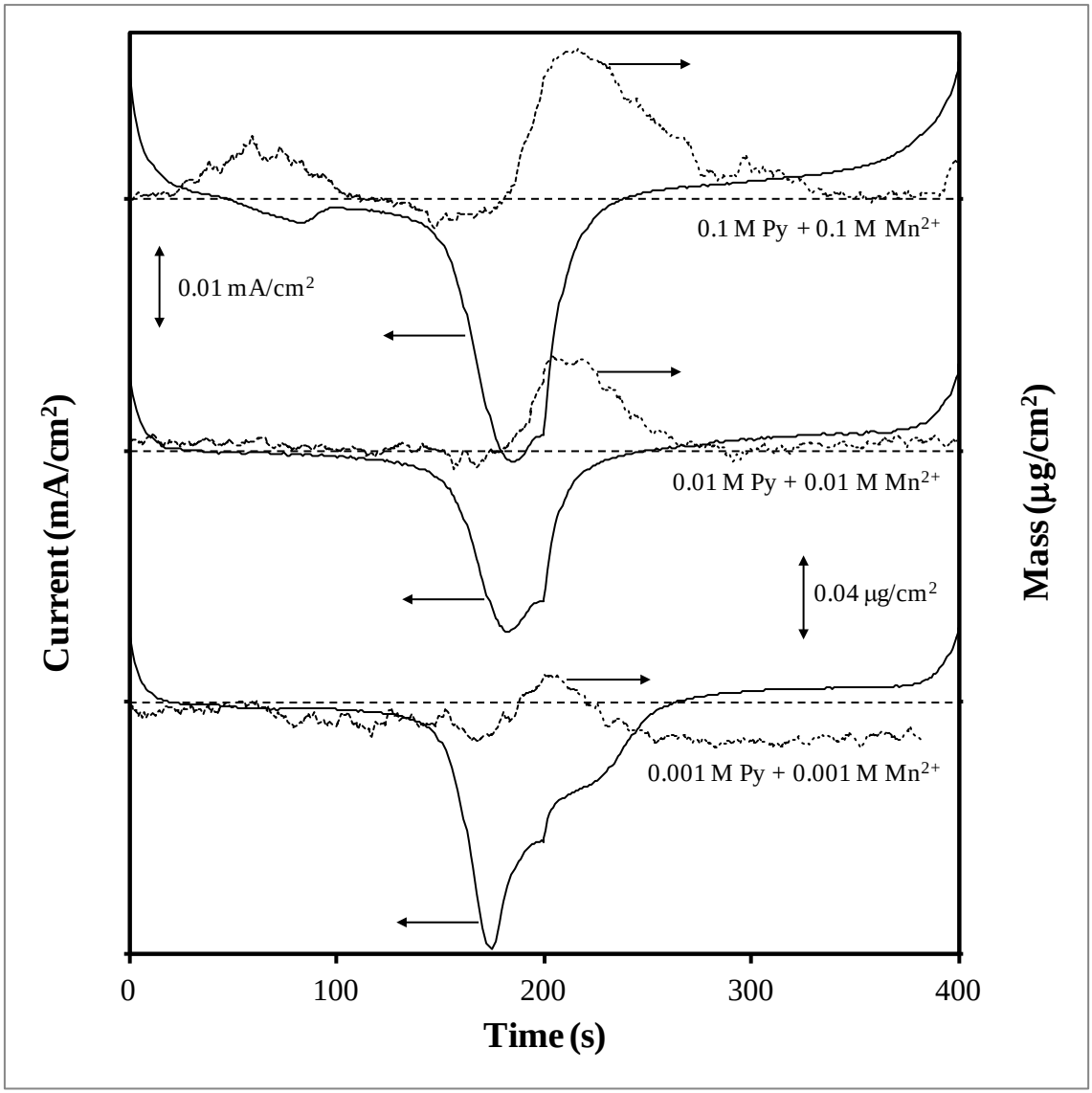
0.1 M Py + 0.1 M Mn2+
0.01 mA/cm2
0.01 M Py + 0.01 M Mn2+
0.04 µg/cm2
0.001 M Py + 0.001 M Mn2+
Current (mA/cm2)
Mass (µg/cm2)
0
100
200
300
400
Time (s)

(b)

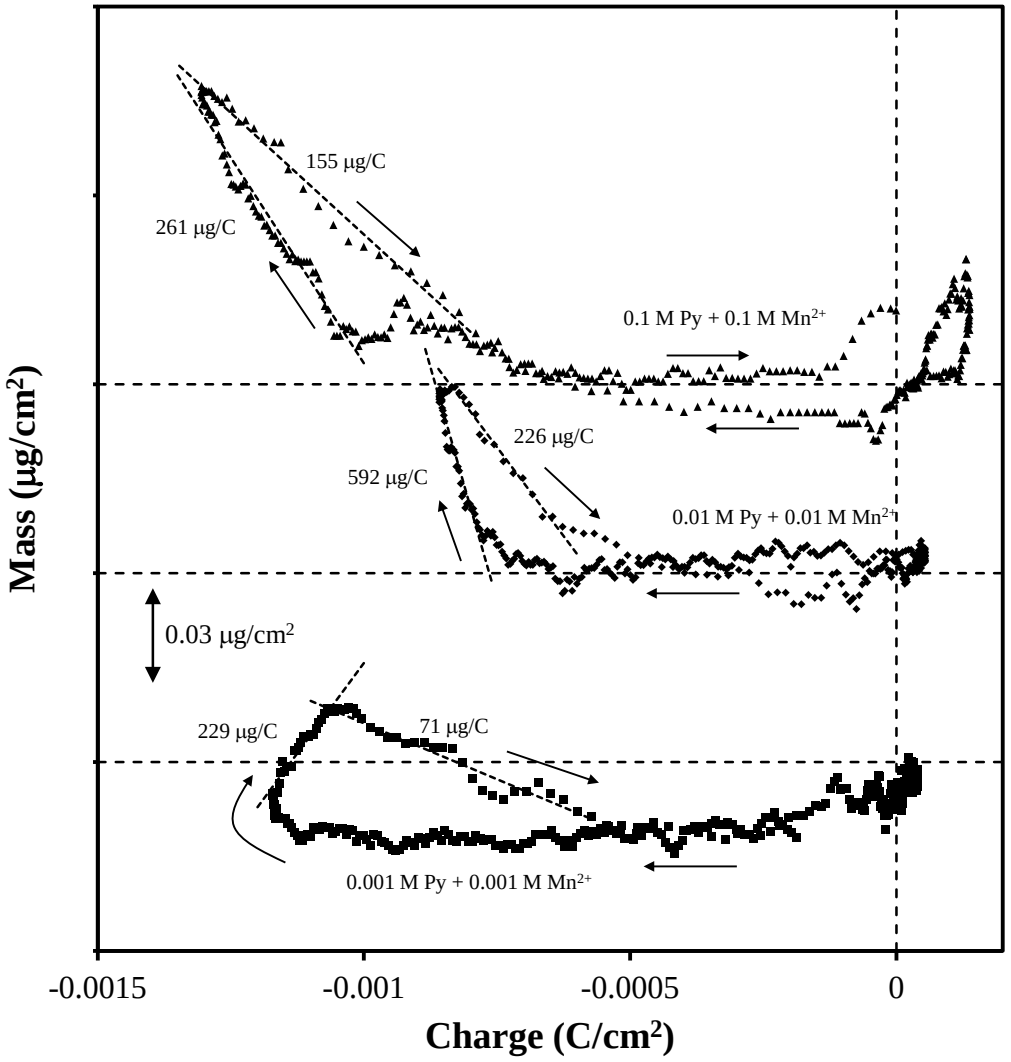

Figure 12. (a) Comparison between the cyclic voltammetry and EQCM massogram data for each of the thin electrode films prepared in this work. (b) Mass versus charge data for the same electrodes. Platinum substrate; 0.1 M K_2SO_4 electrolyte; scan rate = 5 mV/s; data from the 50^{th} cycle.

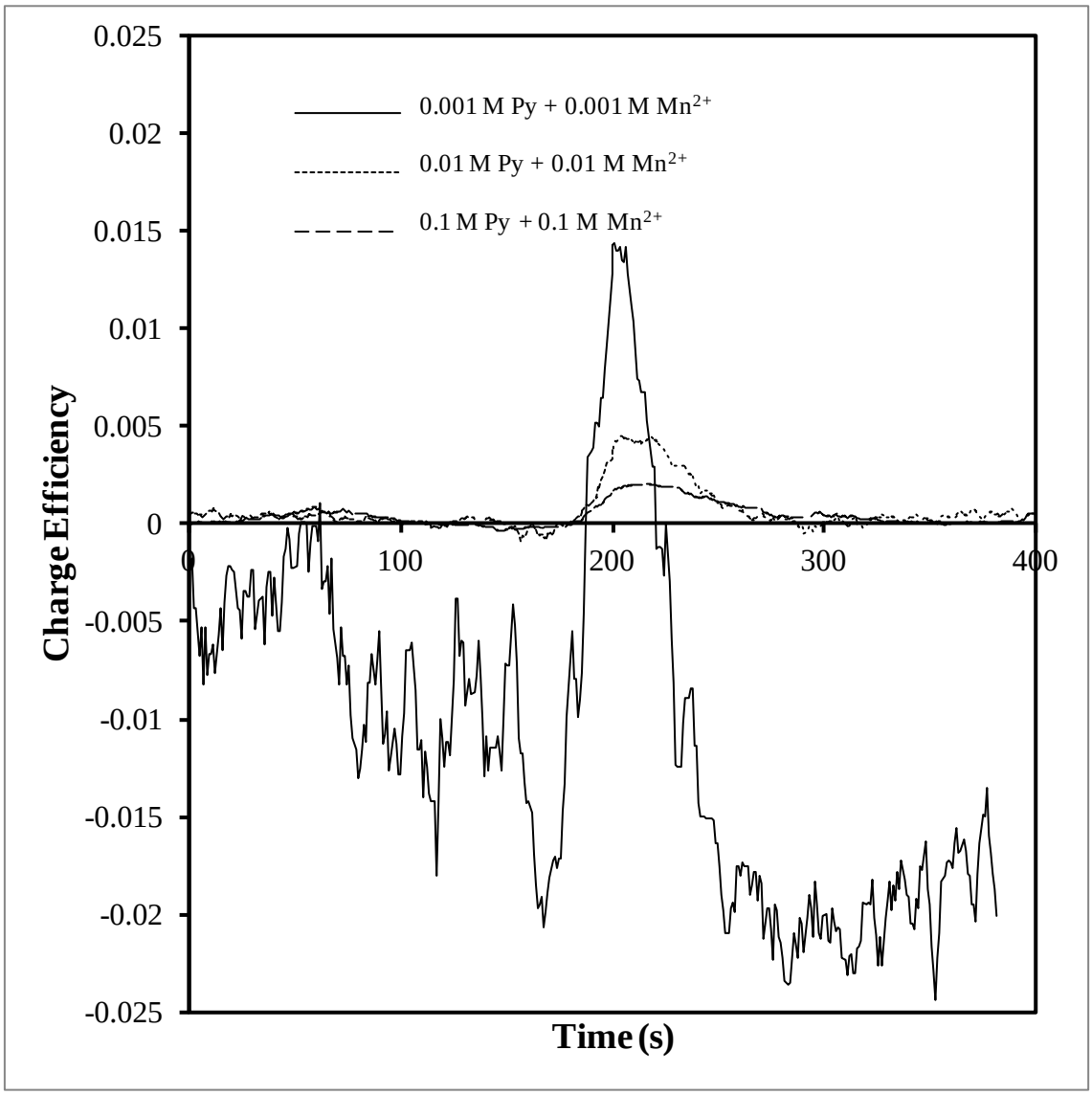

Figure 13. Charge efficiency, expressed as the ratio between the electrode mass change and the starting mass, for each of the thin film electrodes prepared in this work.

(a)

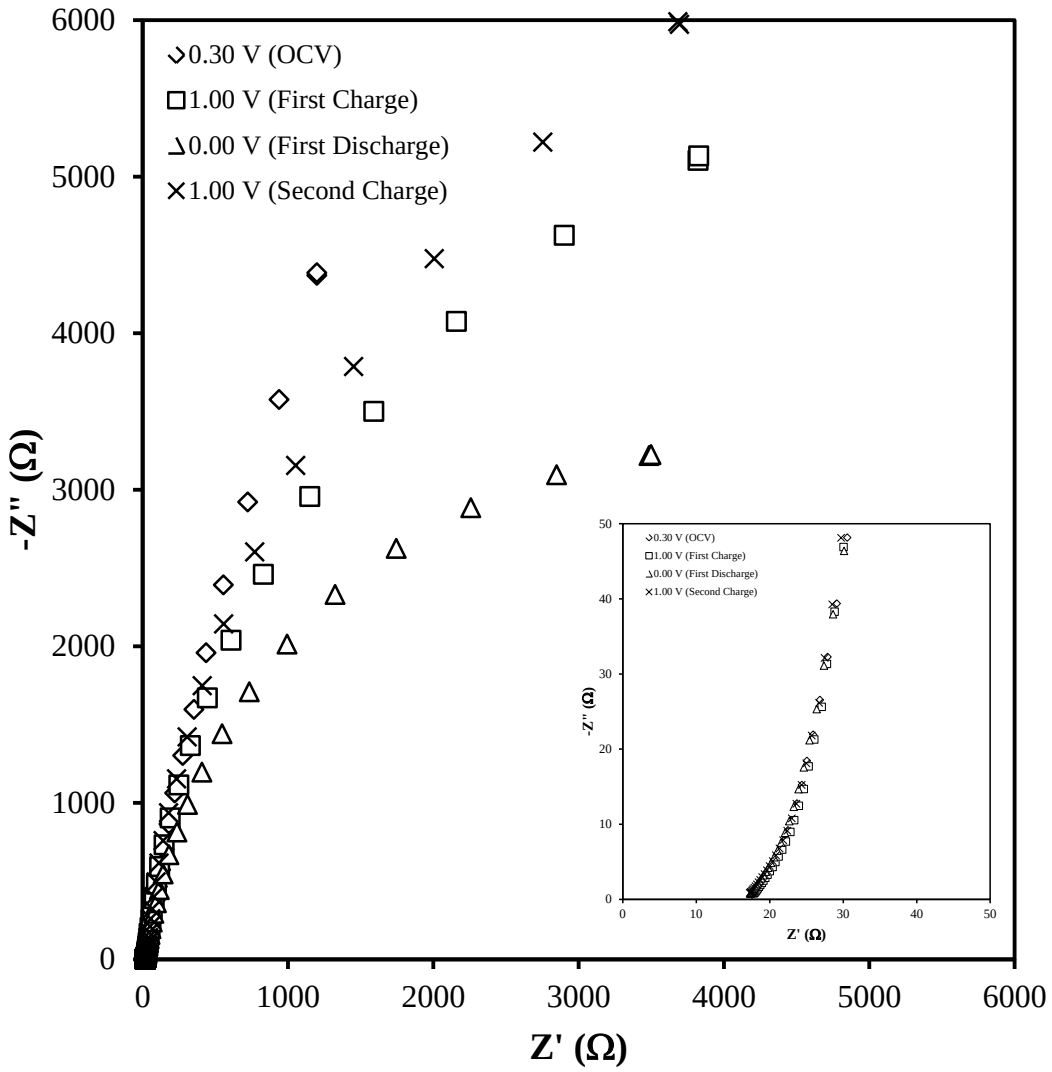

(b)

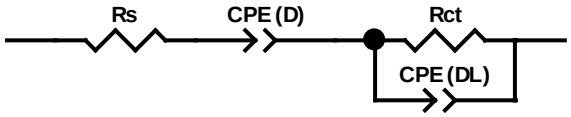

Figure 14. (a) Sample of the EIS data collected, in this case for the thin film electrode prepared from the 0.001 M Py + 0.001 M Mn^{2+} in 0.1 M H_2SO_4 electrolyte. Inset: Expanded view of the high frequency EIS data. **(b)** Equivalent circuit used for modelling the experimental data.